Spatiotemporal mapping of ORC1 reveals its chromatin binding landscape and function in endogenous retrovirus silencing

Ruxin Zhang[1, 2, 5], Xiaoting Zhang[2, 5], Ning Wang[3, 5], Wenchang Gao[2], Minyu Chen[2], Xueqing Ba[3], Haoyue Zhang[2], Zengqi Wen[4 *], Haizhen Long[2 *]

1 School of Basic Medical Sciences, Capital Medical University, Beijing 100069, China.

2 Institute of Molecular Physiology, Shenzhen Bay Laboratory, Shenzhen, 518132, China.

3 Key Laboratory of Molecular Epigenetics of the Ministry of Education (MOE), Northeast Normal University, 5268 Renmin Street, Changchun, Jilin, 130024, China.

4 School of Medicine, Shenzhen Campus of Sun Yat-Sen University, Sun Yat-Sen University, Shenzhen, Guangdong, 518107, China.

5 These authors contributed equally to this work

* Correspondence: longhaizhen@szbl.ac.cn; wenzq7@mail.sysu.edu.cn

Abstract

Origin Recognition Complex subunit 1 (ORC1) is essential for ORC assembly at sequence-independent mammalian origins and regulates diverse epigenetic functions. Thus, mapping its genomic distribution is critical to elucidate the mechanisms underlying mammalian replication origin selection and its broader epigenetic roles. However, existing genomic profiles exhibit considerable variation due to inherent technical challenges. To address this, we generated a mouse embryonic stem (mES) cell line with an HA-MNase-mAID tag knocked into the endogenous *Orc1* locus and optimized a ChEC-seq approach to map ORC1 chromatin binding with high specificity and reproducibility. Our profiling identified approximately 70,000 ORC1 binding sites broadly distributed across euchromatin and heterochromatin, spanning both early- and late-replicating regions. Intriguingly, cell-cycle-resolved profiling revealed that the ORC1 binding landscape remains remarkably stable, including in S phase. Through repli-ChEC-seq, we found that ORC1 rapidly recovers chromatin binding following DNA replication. Despite this persistent chromatin occupancy, ORC1 is dispensable for S phase progression in mES cells. Instead, we uncovered that ORC1 is involved in the epigenetic inheritance of H3K9me3 and the transcriptional repression of endogenous retroviruses (ERVs). Together, these findings provide a comprehensive spatiotemporal binding map of ORC1 in mES cells, and support the expansion of ORC1's functional repertoire ranging from canonical DNA replication to heterochromatin maintenance and ERV silencing.

Main

The accurate transmission of genetic information relies on the precise regulation of DNA replication. DNA replication initiates at replication origins, which are selected by origin recognition complex (ORC) across the genome during G1 phase[1]. In budding yeast, replication origins are defined by conserved autonomously replicating sequence (ARS) elements[2]. In contrast, mammalian replication origins lack consensus sequences[3]. Consequently, the mechanisms by which ORC specifies replication origins across the complex mammalian genome remain a fundamental open question. ORC consists of six subunits, ORC1 to ORC6[4]. ORC1 is the largest subunit, and its association with chromatin is essential for ORC assembly and subsequent origin licensing[5-7]. Furthermore, ORC1 exhibits more dynamic, cell cycle-regulated chromatin binding in mammalian cells than other core ORC subunits[7-10]. Beyond its canonical role in DNA replication, emerging evidence also links ORC1 to broader epigenetic regulation[11]. It directly interacts with HP1 and SUV39H1, participating in heterochromatin regulation and transcription repression[12,13]. Additionally, ORC1 has been implicated in a wide variety of biological processes, including centriole and centrosome duplication[14], nucleosome remodeling via chromatin remodeler interactions[15,16], and the transcriptional regulation of HIV latency[17]. Despite its multifaceted functions, the high-resolution, genome-wide spatiotemporal dynamics of ORC1 across the cell cycle have yet to be fully elucidated. Characterizing the dynamic chromatin occupancy of ORC1 is therefore critical for deciphering its roles in replication origin selection and broader biology functions.

Although several studies have provided valuable insights into the genomic distribution of ORC1, the reported binding landscapes vary considerably, likely reflecting discrepancies in experimental methodologies and cellular contexts. For instance, conventional ChIP-seq targeting endogenous ORC1 in low-density chromatin fractions from HeLa S3 cells yielded approximately 13,000 binding sites[18]. In contrast, our previous work employing overexpressed, biotin-tagged ORC1 in HeLa cells identified roughly 100,000 sites[19]. Furthermore, a recent ChEC-seq analysis in HCT116 cells detected a highly restricted set of only a few thousand ORC1 peaks—with just 710 sites conserved across independent clones—in contrast to the broad genomic distributions observed for the ORC2 (67,525 sites) and ORC5 (36,617 sites) subunits in the same study[20]. This profound variability highlights the inherent technical challenges associated with mapping ORC1 chromatin occupancy. Consequently, there is a pressing need for robust, orthogonal validation strategies to accurately define the baseline ORC1 binding landscape and, ultimately, to resolve its spatiotemporal dynamics across the cell cycle.

To overcome previous technical limitations and accurately map the genomic distribution of endogenous ORC1, we knocked an HA-MNase-mAID tag into the N-terminus of the *Orc1* locus in mouse embryonic stem (mES) cells. We systematically evaluated ORC1 chromatin binding using HA-ChIP-seq, HA-CUT&Tag, and ChEC-seq. Among these orthogonal approaches, ChEC-seq yielded data of the highest-quality, enabling the robust identification of approximately 70,000 ORC1

binding sites in mES cells. The specificity and reliability of these peaks were rigorously validated through multiple controls, including technical and clonal replicates, free MNase expression, pseudo-cleavage, and targeted auxin-induced degradation of ORC1. By subsequently performing ChEC-seq across distinct cell cycle stages, we successfully resolved the genome-wide spatiotemporal dynamics of ORC1 in mES cells. Our analysis revealed that ORC1 is robustly recruited to both euchromatin and heterochromatin, indicating that local chromatin states and ORC1 occupancy cooperatively govern replication origin selection and temporal activation.

Intriguingly, beyond its canonical function in DNA replication, we uncovered a replication-independent role for ORC1 in the epigenetic silencing of endogenous retroviruses (ERVs) in mES cells. Specifically, we demonstrate that ORC1 is required for the epigenetic inheritance of H3K9me3 at ERV loci in mES cells.

Results

ChEC-seq maps endogenous ORC1 binding with high specificity and robustness

To profile endogenous ORC1 binding, we utilized CRISPR-Cas9 to introduce an N-terminal 6×HA-MNase-mAID tag into the 5' of endogenous *Orc1* locus in mES cells (Fig. 1a). Successful integration was confirmed by Sanger sequencing and western blotting (Extended Data Fig. 1a). Comprehensive functional validation — including RNA-seq, Repli-seq, and flow cytometry — demonstrated that this editing did not perturb the expression of DNA replication factors, genome-wide replication timing, or cell cycle progression (Extended Data Fig. 1b-1e).

Using these engineered cells, we systematically compared ChIP-seq, CUT&Tag, and chromatin endogenous cleavage sequencing (ChEC-seq) for mapping ORC1 genomic binding profile (Fig. 1a). While HA-ChIP-seq failed to yield significant signal enrichment and HA-CUT&Tag exhibited a low signal-to-noise ratio, ChEC-seq which maps chromatin-associated proteins under native conditions without relying on antibodies[21], produced well-defined ORC1 binding peaks with superior signal-to-noise ratios (Fig. 1b). This enhanced sensitivity was further reflected by higher Fraction of Reads in Peaks (FRiP) scores (Fig. 1c). Additionally, the insert size distribution of the ChEC-seq libraries displayed a characteristic mono-nucleosomal pattern, indicative of highly specific, localized chromatin cleavage (Extended Data Fig. 1f).

To evaluate the robustness, we performed ORC1 ChEC-seq across two independent knock-in clones. Both technical and biological replicates exhibited high reproducibility and strong quantitative correlations (Fig. 1d and Extended Data Fig. 1g). Importantly, free-MNase and 0-minute pseudo-cleavage controls lacked these distinct signal patterns and yielded low FRiP values (~3%), in contrast to the robust enrichment (>8%) observed in all ORC1 ChEC-seq replicates (Extended Data Fig. 1h). By merging three biological replicates from clone #1 and performing MACS2 peak calling, we identified 69,290 high-confidence ORC1 binding sites for downstream analysis. Finally, to

rigorously validate signal specificity, we acutely degraded the 6×HA-MNase-mAID-ORC1 fusion protein using 5-Ph-IAA (Extended Data Fig. 1i). ORC1 ChEC-seq signals progressively diminished upon protein depletion (Fig. 1e), and genome-wide quantification at the identified peaks confirmed a concordant, targeted reduction (Fig. 1f), firmly establishing that the ChEC-seq signals are strictly dependent on endogenous ORC1 occupancy.

ORC1 binding density, rather than individual peak intensity, correlates with replication timing

We next examined the genome-wide distribution of ORC1 and its relationship to DNA replication. ORC1 peaks were broadly distributed across intergenic regions (44.21%), introns (29.82%), and promoters (17.18%) (Fig. 2a). To evaluate ORC1 occupancy at functional origins, we integrated our data with publicly available short nascent strand sequencing (SNS-seq)[22] and Okazaki fragment sequencing (OK-seq) datasets[23] from mES cells, which define localized replication origins and broader initiation zones (IZs), respectively. While ORC1 peaks showed partial direct overlap with SNS-seq peaks (Fig. 2b), SNS-seq signals were highly enriched around ORC1 binding sites (Fig. 2c). Furthermore, almost all of OK-seq-derived IZs contain at least one ORC1 peak (Fig. 2d). Notably, the replication fork directionality (RFD) profile centered on ORC1 binding sites closely mirrored the transitions observed at established IZs (Fig. 2e). Consistent with our previous finding in HeLa cells that H2A.Z promotes ORC1 recruitment via H4K20me2 to activate early origins[19], both H2A.Z and H4K20me2 were highly enriched at ORC1 binding sites in mES cells (Extended Data Fig. 2a-2b). Additionally, ORC1 signals were prominently enriched at ERCEs (Extended Data Fig. 2c), which was defined as early replicating control elements[24]. Collectively, these data confirm that active replication initiation loci are robustly associated with ORC1 binding.

We next investigated how ORC1 binding relates to the temporal regulation of DNA replication initiation. While the majority (68.4%) of ORC1 binding sites were located within early and middle-early replicating regions (Fig. 2f), substantial ORC1 occupancy was also observed in late-replicating domains (Fig. 2f-2g). Surprisingly, absolute ORC1 signal intensities did not differ markedly across peak groups with distinct replication timing (RT) profiles (Extended Data Fig. 2d), and intra-peak ORC1 signal showed no correlation with global RT values ($r^2 = -0.02$) (Fig. 2h). In fact, ORC1 signal intensities at late IZs were slightly higher than those at early IZs (Extended Data Fig. 2e). However, when evaluating the spatial distribution of these binding sites, we found that early IZs contained significantly more ORC1 peaks than late IZs (Fig. 2i). A similar trend was observed across larger Repli-seq–defined RT domains, where early domains harbored a markedly higher density of ORC1 peaks compared to late domains (Extended Data Fig. 2f). Together, these results suggest that although ORC1 supports replication across all temporal domains, the precise timing of replication likely depends on the spatial clustering of ORC1 binding sites rather than the strength of individual ones. This clustered regulation model is consistent with the stochastic nature of replication initiation in mammals[25].

ORC1 occupies both euchromatic and heterochromatic domains with distinct replication timing profiles

Given the intimate link between replication timing and chromatin states, we next investigated the epigenetic landscape of ORC1 binding sites. Broadly, ORC1 exhibited strong colocalization with accessible chromatin (ATAC-seq peaks) and active histone marks, including H3K4me3, H3K9ac, and H3K27ac, alongside partial overlap with the repressive marks H3K9me3 and H3K27me3 (Fig. 3a). To evaluate this quantitatively, we stratified ORC1 peaks into quintiles (Q1-Q5) based on decreasing signal intensity. We found that ORC1 signal positively correlated with euchromatic features (ATAC, H3K4me3, H3K9ac, and H3K27ac) and gene expression level, but not with H3K4me1, H3K9me3, or H3K27me3 (Extended Data Fig. 3a).

While these initial analyses suggested a general preference for open chromatin, unsupervised clustering of ORC1 peaks based on epigenetic signatures revealed a more complex, partitioned distribution. Beyond the expected enrichment of euchromatic marks—specifically H3K4me3 (cluster 3), H3K27ac (cluster 7) and ATAC (cluster 5)—we identified a large, distinct cluster of ORC1 peaks uniquely characterized by H3K9me3 enrichment (cluster 2) (Fig. 3b). Although the average ORC1 signal intensity within this H3K9me3-associated cluster was slightly lower than in the euchromatic groups (Fig. 3c), no substantial differences were observed in the number of ORC1 peaks within IZs across these clusters (Fig. 3d). However, H3K9me3-ORC1 regions exhibited significantly delayed replication timing compared to their euchromatic counterparts (Fig. 3e), aligning directly with the established late-replicating nature of heterochromatin[26]. Collectively, these findings demonstrate that ORC1 is robustly recruited to both euchromatin and heterochromatin. Together, these results suggested that replication timing is dictated by the local epigenetic environment, other than ORC1 occupancy.

Cell cycle profiling of ORC1 reveals continuous chromatin association and M-to-G1 spatial redistribution in mES cells

While ORC1 protein levels exhibit well-characterized, cell cycle–dependent fluctuations in mammalian cells, its spatiotemporal genomic distribution across the cell cycle remains poorly defined. Using our engineered 6×HA-MNase-mAID-ORC1 mES cells, we synchronized cells in M phase and monitored ORC1 chromatin-binding dynamics over an 8-hour time course via western blotting and immunofluorescence (Fig. 4a-4d). Strikingly, in contrast to the robust S-phase degradation of ORC1 observed in HeLa and HEK293T cells—both in our current study (Extended Data Fig. 4a-4b) and in previous reports[8,27]—mES cells exhibited only a modest reduction in chromatin-bound ORC1 during S phase (Fig. 4b and Extended Data Fig. 4c-4d). Immunofluorescence analysis further confirmed this persistent chromatin association (Fig. 4c-4d).

To map the cell cycle binding profiles, we performed ChEC-seq at G1, S, and G2/M phases after

releasing cells from nocodazole-induced metaphase arrest (Fig. 4a and Fig. 4e). Consistent with our cytological and biochemical observations, genomic ORC1 signals remained highly correlated across all three cell cycle stages, confirming its sustained chromatin binding throughout S phase (Fig. 4e and Extended Data Fig. 4e-4f). Using the ORC1 peaks identified in asynchronous cells as a reference, we defined 49,315, 48,241, and 55,430 high-confidence ORC1 peaks in the G1, S, and G2/M phases, respectively, by filtering out the lowest 10% of signals based on their fold enrichment over corresponding 0-minute pseudo-cleavage controls (Extended Data Fig. 4g). These peaks displayed extensive overlap (Fig. 4e-4f), indicating that the global ORC1 binding landscape is largely preserved throughout the mES cell cycle.

It's reported that ORC1 loading continues from metaphase to G1 phase in human cells[7,10]. We also examined its binding dynamics during this transition. By conducting differential binding analysis, we categorized ORC1 peaks as G1-specific, G2/M-specific, or shared (Fig. 4g and Extended Data Fig. 4h). Notably, compare with G2/M-specific peaks, G1-specific peaks showed substantial decrease in promoter binding, and increase in intergenic binding (Fig. 4h). These results suggested a spatial redistribution of ORC1 during M-to-G1 transition—specifically, a partial disassociation from promoters coupled with increased loading at intergenic sites.

Previously, we defined ORC1 peak clusters with distinct epigenetic features (Fig. 3b). We next examined the dynamics of these ORC1 clusters through cell cycle stages. Aligning with the observed reduction in promoter occupancy, euchromatic ORC1 peaks, including those marked by H3K4me3, H3K27ac, and ATAC accessibility, consistently exhibited decreased signal during M-to-G1 transition (Fig. 4i). Remarkably, the signals at H3K9me3-ORC1 peaks remained relatively stable across all cell cycle stages (Fig. 4i).

Together, these results revealed that ORC1 globally maintains chromatin binding pattern during cell cycle in mES cells, while re-distributes at certain genomic regions, most notably loss of binding at some promoters during M-to-G1 transition.

ORC1 recovers chromatin binding rapidly after DNA replication

Given our observation that ORC1 maintains its genome-wide binding pattern throughout S phase (Fig. 4), we next asked whether ORC1 recover chromatin binding following DNA replication. To this end, we pulse-labeled nascent DNA with the nucleoside analogue EdU (5-Ethynyl-2'-deoxyuridine) prior to ChEC-seq, establishing a "repli-ChEC-seq" approach to map ORC1 binding dynamics specifically on nascent chromatin (Fig. 5a). We found that while ORC1 transiently dissociates from chromatin during the passage of the replication fork, it rapidly re-binds to nascent chromatin (Fig. 5b-5c). At the ensemble level, global ORC1 binding was largely restored within 2 hours post-replication, with no further signal accumulation observed at the 4-hour or 8-hour time points (Fig. 5b-5c). Using a reported quantitative framework[28], we classified the ORC1 peaks into

four temporal recovery categories: R0.5, R1, and R2 (representing robust recovery at 0.5, 1, and 2 hours, respectively), alongside an "unstable" group, which exhibits more dynamic, fluctuating recovery behavior (Fig. 5d-5e).

We next evaluated the interplay between ORC1 recovery kinetics and various genomic features, including spatial distribution, transcription levels, replication timing (RT), and epigenetic states. Surprisingly, although the four temporal groups (R0.5, R1, R2, and unstable) represent distinct recovery kinetics, their genomic distribution patterns were remarkably similar (Extended Data Fig. 5a). Consistent with this, ORC1 peaks located within intergenic regions, introns, and promoters displayed globally comparable recovery trajectories, with promoter-associated peaks recovered marginally faster (Fig. 5f). When stratifying promoter-bound ORC1 peaks by the expression levels of their associated genes, recovery rates remained largely uniform, with only a modestly accelerated recovery observed at the most highly expressed genes (Fig. 5g). Similarly, when peaks were partitioned into early, mid-early, mid-late, and late RT groups, the recovery kinetics were highly consistent across all temporal domains, with early-replicating peaks recovering only slightly faster (Fig. 5h). Consequently, these four RT groups contained nearly identical proportions of the R0.5, R1, R2, and unstable recovery categories (Extended Data Fig. 5b). Finally, while H3K4me3-, ATAC-, and H3K27ac-ORC1 peaks exhibited near-identical recovery rates, H3K9me3-ORC1 peaks recovered at a slightly slower rate (Fig. 5i). Accordingly, the distribution of the four recovery categories was highly consistent across all four epigenetic clusters of ORC1 (Extended Data Fig. 5c). Together, these results demonstrate that ORC1 undergoes rapid post-replication chromatin recovery, which operates largely independently of local genomic distribution, transcription, replication timing, or epigenetic states.

ORC1 is dispensable for DNA replication progression during S Phase

To determine whether the continuously retained ORC1 actively regulates DNA replication during S phase, we developed a strategy for acute protein depletion specifically at the G1/S boundary. As combining mAID and Bromo tags has been shown to enhance ORC1 degradation efficiency[29], we introduced a Bromo-tag into our existing 6×HA-MNase-mAID-ORC1 mES cell line. We then synchronized these cells at the G1/S transition, induced rapid ORC1 degradation using 5-Ph-IAA and AGB1, and released them into S phase to monitor replication progression (Fig. 6a). Flow cytometry analysis revealed that acute ORC1 degradation at the G1/S boundary did not impair progression through the ongoing S phase (Fig. 6b-6c). However, continuous tracking demonstrated that ORC1 loss induced profound defects in the subsequent cell cycle stages, including G2/M arrest and delayed entry into the next S phase (Fig. 6b-6c). These secondary defects align with the cell cycle arrest observed following prolonged ORC1 depletion in asynchronous populations (Extended Data Fig. 6a-6b).

Biochemical analysis further supported this uncoupling of ORC1 from DNA replication in S phase.

While ORC1 depletion in asynchronous cells severely reduced global MCM complex loading (Fig.6d and Extended Data Fig. 6c), targeted depletion at the G1/S boundary had no effect on total chromatin-bound MCM levels or MCM2 phosphorylation upon release into S phase, indicating that origin activation remained un-affected (Fig. 6d). To assess replication dynamics at the single-molecule level, we performed DNA fiber assays. Consistent with our biochemical data, the acute loss of ORC1 in S-phase did not impede replication fork progression; rather, it resulted in a marginal increase in fork progression speed (Fig. 6e-6f).

Together, these results demonstrate that although ORC1 remains abundantly associated with chromatin throughout S phase in mES cells, it is largely dispensable for ongoing DNA replication and fork progression once origins have fired. This aligns with the established paradigm that ORC1 functions to license replication origins exclusively during the G1 phase[30].

ORC1 Regulates H3K9me3 inheritance and ERV Silencing during S Phase

Given that ORC1 co-localizes with H3K9me3 across the genome (Fig. 3a-3b) and interacts with HP1 and SUV39H1[12,13], we asked whether ORC1 contributes to the regulation of H3K9me3-marked heterochromatin during S phase. To explore this, we synchronized cells at the G1/S boundary, induced rapid ORC1 degradation using 5-Ph-IAA and AGB1, and then released the cells into mid S phase as described previously (Fig. 6a). Immunofluorescence analysis revealed that, during S phase, ORC1 formed punctate nuclear foci that strongly co-localized with H3K9me3 and DAPI-dense heterochromatin (Fig. 7a-7b). Upon ORC1 depletion, both nuclear H3K9me3 and DAPI signals were reduced and appeared more diffuse (Fig. 7a and Fig. 7c). A similar phenomenon was also observed in asynchronous cell populations (Extended Fig. 7a-7c). While ORC1 depletion only mildly impacted global H3K9me3 levels (Extended Fig. 7d), it substantially delayed the recovery of global H3K9me3 on nascent chromatin (Extended Fig. 7e), particularly at H3K9me3-ORC1 co-localized regions (Fig. 7d). Interestingly, within these H3K9me3-ORC1 colocalization regions, ORC1 recovered more rapidly than H3K9me3 based on the recovery rate at the 1-hour chasing point (Fig. 7e and Extended Fig. 7e-7f), and its depletion severely impaired H3K9me3 restoration (Fig. 7e). These results indicate that ORC1 facilitates the inheritance of H3K9me3 during chromatin replication.

H3K9me3 plays a critical role in silencing transposable elements and thereby maintaining genome stability in mouse ES cells[31]. Notably, 66% of H3K9me3-ORC1 co-localized regions overlap with repetitive elements, with 41% specifically mapping to endogenous retroviruses (ERVs) (Fig. 7f). Further analysis identified four Class II and one Class I ERV subfamilies as the most enriched subfamilies within these regions[32] (Fig. 7g). Notably, ERV-associated H3K9me3-ORC1 regions exhibited higher baseline H3K9me3 levels compared to non-ERV regions (Fig. 7h). Upon ORC1 depletion, H3K9me3 levels decreased uniformly across these H3K9me3-ORC1 regions (Fig. 7h), with a consistent reduction observed among these highly enriched ERV subfamilies (Fig. 7i).

Since H3K9me3 is known to repress ERV transcription[31], we next investigated whether ORC1 depletion impacts ERV expression. While TT-seq analysis indicated that global gene expression remained largely unaffected in asynchronous cells (Extended Fig. 7g), ERVs located within H3K9me3-ORC1 domains exhibited significantly elevated transcription upon ORC1 depletion (Fig. 7j and Extended Fig. 7h).

Together, these results demonstrate that ORC1 promotes the inheritance of H3K9me3 during chromatin replication in mES cells. Through this mechanism, ORC1 contributes to heterochromatin maintenance and ERV silencing, as highlighted by the *Malrd1* locus (Fig. 7k).

Discussion

ORC1, the largest core subunit of the origin recognition complex (ORC), is essential for ORC assembly and replication licensing, while also participating in diverse cellular processes beyond DNA replication. Consequently, precisely mapping its genomic distribution is crucial. However, profiling endogenous mammalian ORC1 binding remains challenging due to its dynamic behavior and the scarcity of ChIP-grade antibodies. To address this, we engineered mES cells with endogenously tagged ORC1 (6×HA-MNase-mAID) and systematically compared HA-ChIP-seq, HA-CUT&Tag and ChEC-seq. We found that ChEC-seq, which relies on in vivo DNA cleavage by the ORC1-fused MNase, produced binding profiles with the highest signal-to-noise ratio. The specificity of this approach was confirmed by the absence of peak-like signals following exogenous MNase treatment, as well as the near-complete loss of ChEC-seq signals upon auxin-induced ORC1 degradation. Together with the high reproducibility observed across independent clones and biological replicates, these results demonstrate the robustness, specificity, and reliability of our genomic data.

Unlike budding yeast, mammalian replication origins lack a defined consensus sequence, leaving the mechanisms of ORC-mediated origin selection largely unclear. In this study, we found that while a subset of ORC1 peaks overlaps with active origins—as defined by SNS-seq, OK-seq, and ERCEs—the majority of ORC1-bound sites lack detectable origin activity. This discrepancy indicates that ORC1 occupancy alone is insufficient to specify functional origins. Rather, ORC1 establishes a broad landscape of potential initiation sites whose actual utilization is dictated by the local chromatin context. Furthermore, while individual ORC1 signal intensities are comparable between early- and late-replicating domains, early domains exhibit a significantly higher density of ORC1 binding sites, consistent with previous reports of increased ORC2 occupancy in early domains of human K562 erythroid cells[33].This suggests that the spatial density of ORC binding, rather than isolated peak strength, drives replication timing.

Because mammalian ORC binding is largely sequence-independent, distinct chromatin

environments likely govern ORC1 function through different recruitment pathways. For example, our previous work showed that H2A.Z recruits ORC1 via H4K20me2 to promote early origin activity[19]. Conversely, we now demonstrate that a subset of ORC1 localizes within H3K9me3-marked heterochromatin and is linked to late replication, implying a heterochromatin-specific recruitment mode. Collectively, these findings support a model wherein ORC1 delineates potential origins, while the chromatin landscape regulates their activation probability and timing. Thus, ORC1 and chromatin context act in concert to shape the spatiotemporal replication program.

Although global ORC1 binding in mES cells remained broadly consistent across the cell cycle, we observed temporal redistributions, such as reduced promoter occupancy in G1 phase. This phenomenon is also observed in budding yeast[34], indicating that this persistence is evolutionarily conserved. Strikingly, ORC1 regulation in mES cells diverges fundamentally from that in human somatic cells: rather than undergoing robust S-phase degradation, mES-derived ORC1 exhibits continuous retention and rapid post-replication reloading onto chromatin. Acute S-phase depletion revealed that this retained ORC1 is largely dispensable for ongoing DNA synthesis and replication fork progression once origins have fired. Instead, we uncovered an unexpected requirement for ORC1 in the maintenance of epigenetic state. Specifically, S-phase ORC1 loss compromised H3K9me3 inheritance and thus disrupted global heterochromatin organization. Because H3K9me3-ORC1 co-occupied regions are highly enriched for endogenous retroviruses (ERVs), this structural disruption directly triggered ERV de-repression. Together, these findings uncouple the post-initiation role of ORC1 from DNA replication, highlighting a non-canonical function for ORC1 in heterochromatin maintenance and ERV silencing in mES cells. Whether this mechanism still functions in differentiated cells remains to be further investigated.

In summary, our study delineates the dynamic genomic landscape of ORC1 in mouse embryonic stem cells. We demonstrate that while ORC1 broadly defines potential replication origins, isolated binding intensity alone does not dictate replication timing. Instead, the spatial clustering of ORC1 and the local chromatin environment act in concert to govern the spatiotemporal replication program. Furthermore, we revealed that ORC1 regulates epigenetic inheritance of H3K9me3 heterochromatin and ERV silencing during S phase. By uncoupling its post-initiation role from DNA synthesis, our findings bridge ORC1 dynamics with both replication origin selection and heterochromatin regulation, providing new insights into its multifaceted role in safeguarding genome and epigenome integrity.

Methods:

Knock-in mouse ES cell lines construction

The source and passage of Mouse embryonic stem (mES) cell line R1 were as previously described[35]. mES cells were cultured in medium containing 80% DMEM (Gibco, C11995500BT), 15% FBS (Sigma-Aldrich, F8318), nonessential amino acids (EmbryoMax, TMS-001-C), 2-mercaptoethanol (EmbryoMax, ES-007-E), L-glutamine (EmbryoMax, TMS-002-C), nucleosides (EmbryoMax, ES-008-D), penicillin/streptomycin (EmbryoMax, TMS-AB-2C), and 1000 U/ml leukemia inhibitory factor (LIF) (Novoprotein, C690). Cells were maintained at 37 °C in a humidified incubator with 5% CO_2.

To generate 6×HA-MNase-mAID-ORC1 or 6×HA-MNase-mAID-bromo-ORC1 knock-in mouse ES cell lines, we first established a stable V5-osTIR1(F74G)-overexpressing cell line via lentiviral transduction, followed by neomycin selection to obtain single clones. The V5-osTIR1(F74G) stable cells were then co-transfected with the pX330-sgORC1 plasmid, a donor plasmid containing either the 6×HA-MNase-mAID or 6×HA-MNase-mAID-bromo tag flanked by homologous arms surrounding the start codon, and a pCAG-EGFP plasmid carrying a puromycin resistance gene. Transfected cells were selected with 1 μg/ml puromycin until single clones were isolated and screened by PCR. Positive clones were further confirmed by DNA sequencing.

The sgORC1 sequence was ATGCTGAACTCCATTAAG.

The primers used for homologous arm amplification from genome were:

Forward: CCATCCTACCTCACAAGGCAG; Reverse: GGTCTGATGGGctgtaagatacag.

The primers used for identify positive clones were:

Forward: ccagggctgtgtaaaagagac; Reverse: ctcaagactttcacaagctccagc.

Chromatin endonuclease cleavage sequencing (ChEC-seq) and repli-ChEC-seq

ChEC-seq was performed as previously described with minor modifications[21]. Native cell pellets were resuspended and incubated on ice for 10 min in buffer A (10 mM Tris-HCl, pH 7.5; 10 mM NaCl; 60 mM KCl; 3 mM $MgCl_2$; EDTA-free protease inhibitor cocktail (Roche, 05892791001); 0.5 mM spermidine (Sigma-Aldrich, S2626); 0.2 mM spermine (Sigma-Aldrich, S3256)) supplemented with 1 mM EDTA and 0.1% NP-40. After centrifugation at 500 × g for 3 min at 4 °C, cells were resuspended and incubated again on ice for 10 min in NB150 buffer (10 mM Tris-HCl, pH 7.5; 150 mM NaCl; 10 mM KCl; 3 mM $MgCl_2$; 0.5 mM spermidine; 0.2 mM spermine; EDTA-free Roche Complete protease inhibitor) supplemented with 1 mM EDTA. Cells were then centrifuged and washed once with buffer A. The resulting cell pellet was further resuspended in buffer A containing 2 mM $CaCl_2$ and incubated at 37 °C for MNase digestion at the indicated time points. The reaction was terminated by adding 2× stop solution (400 mM NaCl, 20 mM EDTA, 4 mM EGTA). Further, DNA was purified by phenol–chloroform extraction and ethanol precipitation. DNA fragments were size-selected using VAHTS DNA Clean Beads (Vazyme, N411) with a two-step 0.4×/1.4× ratio purification to enrich for short fragments. Libraries were prepared using the

VAHTS Universal DNA Library Prep Kit for Illumina V4 (Vazyme, ND610) according to the manufacturer's instructions.

For repli-ChEC-seq, mouse ES cells were pulse-labeled with EdU (Santa Cruz, sc284628) at 20 μM for 30 min. Immediately after labeling, nascent chromatin samples (T0) were collected. The remaining cells were washed twice with PBS and chased in fresh medium containing thymidine (10 μM) at 37 °C until collection at the indicated time points. EdU-labeled mouse ES cells were first processed according to the ChEC-seq protocol described above. The size-selected EdU-labeled DNA was then biotinylated via a 45-min click reaction at room temperature (0.25 mM biotin-azide, 0.5 mM $CuSO_4$, 2.5 mM THPTA, 10 mM sodium ascorbate), followed by quenching with 20 mM EDTA. DNA was purified using 0.9× DNA Clean Beads and eluted in TE buffer. Biotinylated DNA was incubated with MyOne Streptavidin C1 beads (Life Technologies, 65001) in BW buffer (10 mM Tris-HCl, pH 7.5; 0.5 mM EDTA; 1 M NaCl; 0.05% Tween-20) for 30 min at room temperature with rotation. Beads were washed four times with BW buffer, twice with TE buffer, and once with 10 mM Tris-HCl (pH 8.0), and finally resuspended in nuclease-free water. Sequencing libraries were prepared using the VAHTS Universal DNA Library Prep Kit for Illumina V4 and sequenced on a DNBSEQ-T7 (MGI) platform in paired-end 150-bp mode (PE150).

ChIP-seq and ChOR-seq

ChIP-seq was performed as previously described with minor modifications[36,37]. Cells were crosslinked directly in culture dishes with 1% formaldehyde in PBS for 10 min at room temperature and quenched with 125 mM glycine. Cells were scraped, collected, and washed twice with PBS. Cell pellets were resuspended in buffer 1 (50 mM HEPES-KOH, pH 7.5; 140 mM NaCl; 1 mM EDTA; 10% glycerol; 0.5% NP-40; 0.25% Triton X-100; 1 mM PMSF; 1 μg/ml aprotinin; 1 μg/ml leupeptin; 1 μg/ml pepstatin) and rotated for 10 min at 4 °C. Cells were then incubated in buffer 2 (200 mM NaCl; 1 mM EDTA; 0.5 mM EGTA; 10 mM Tris-HCl, pH 8.0) for 10 min at 4 °C with rotation. The resulting pellets were resuspended in nuclei lysis buffer (50 mM Tris-HCl, pH 8.0; 10 mM EGTA; 1% SDS) and sonicated using a Q800R3 sonicator (Qsonica). Sonication was finished until de-cross-linked DNA fragments reached approximately 200–500 bp. For immunoprecipitation, BSA-blocked protein A/G Dynabeads were first incubated with 2.5 μg antibody in RIPA-150 buffer (50 mM Tris-HCl; 150 mM NaCl; 1 mM EDTA; 0.5% Triton X-100; aprotinin, leupeptin, and PMSF) at 4 °C for 8h, then the sonicated chromatin was added with antibody coated Dynabeads in RIPA-150 buffer and incubated overnight at 4 °C with rotation. Beads were sequentially washed three times each with RIPA-150, RIPA-500 (50 mM Tris-HCl; 500 mM NaCl; 1 mM EDTA; 0.5% Triton X-100; protease inhibitors), and RIPA-LiCl (50 mM Tris-HCl, pH 8.0; 1 mM EDTA; 1% NP-40; 0.7% sodium deoxycholate; 0.5 M LiCl). DNA was eluted by incubating beads in elution buffer (10 mM Tris-HCl, pH 8.0; 0.3 M NaCl; 5 mM EDTA; 0.5% SDS) at 65 °C for 1 h with vortexing. The eluted DNA was subsequently de-crosslinked and treated with RNase A and proteinase K. DNA was then purified by phenol–chloroform extraction followed by ethanol precipitation. Sequencing

libraries were prepared using the VAHTS Universal DNA Library Prep Kit for Illumina V4 (Vazyme, ND610) and sequenced on a DNBSEQ-T7 (MGI) platform in paired-end 150-bp mode (PE150).

For ChOR-seq, cells were pulse-labeled with EdU (20 μM) for 10 min. Immediately after labeling, nascent chromatin samples (T0) were collected. The remaining cells were washed twice with PBS and then cultured in fresh medium containing 2mM thymidine at 37 °C until collection at the indicated time points. Drosophila S2 cells were labeled with EdU (20 μM) for 48 h and used as spike-in chromatin controls. EdU-labeled cells were first processed according to the ChIP-seq protocol described above. Purified EdU-labeled DNA was then biotinylated via a 45-min click reaction at room temperature (0.25 mM biotin-azide, 0.5 mM $CuSO_4$, 2.5 mM THPTA, 10 mM sodium ascorbate), followed by quenching with 20 mM EDTA. DNA was purified using 0.9× DNA Clean Beads and eluted in TE buffer. Biotinylated DNA was incubated with MyOne Streptavidin C1 beads (Life Technologies, 65001) in BW buffer (10 mM Tris-HCl, pH 7.5; 0.5 mM EDTA; 1 M NaCl; 0.05% Tween-20) for 30 min at room temperature with rotation. Beads were washed four times with BW buffer, twice with TE buffer, and once with 10 mM Tris-HCl (pH 8.0), and finally resuspended in nuclease-free water. Sequencing libraries were prepared using the VAHTS Universal DNA Library Prep Kit for Illumina V4 (Vazyme, ND610) and sequenced on a DNBSEQ-T7 (MGI) platform in paired-end 150-bp mode (PE150).

Native ChIP-seq

Native ChIP-seq was performed as previously described with minor modifications[19]. Native cell pellets were firstly resuspended in TM2 buffer (20 mM Tris-HCl, pH 7.4, 2 mM $MgCl_2$, and protease inhibitor cocktail) and incubated on ice for 10 min. NP-40 was then added to a final concentration of 1.5%, followed by incubation on ice for an additional 5 min. The cell pellets were washed once with TM2 buffer, resuspended again in the same buffer, supplemented with $CaCl_2$ to a final concentration of 1 mM, and digested with MNase (Sigma-Aldrich, N3755) at a final concentration of 0.25 U/mL at 37 °C for 10 min. The reaction was terminated by adding EGTA to a final concentration of 10 mM, followed by centrifugation to remove the supernatant. The pellet was washed once with TM2 buffer, resuspended in STM600 buffer, and chromatin was extracted by overnight rotation at 4 °C. After high-speed centrifugation, the supernatant was collected. Meanwhile, 2.5 μg of anti-H2A.Z (Abcam, ab4174) or anti-H4K20me2 (Abcam, ab9052) antibody was incubated with BSA-blocked Protein A/G beads at 4 °C for 8h. The chromatin supernatant was then added and incubated with the antibody-bound beads overnight at 4 °C with rotation. The beads were washed five times with STM600 buffer (20 mM Tris-HCl, pH 7.4, 2 mM $MgCl_2$, 600 mM NaCl, 0.1% Triton X-100). DNA was eluted by incubating the beads in elution buffer (10 mM Tris-HCl, pH 8.0, 0.3 M NaCl, 5 mM EDTA, and 0.5% SDS) at 65 °C for 1 h with vortexing. The eluted DNA was then treated with RNase A (Sigma-Aldrich, R6513) and proteinase K (Sigma-Aldrich, R2308), followed by purification by phenol–chloroform extraction and ethanol precipitation. Sequencing libraries were prepared using the VAHTS Universal DNA Library Prep Kit for Illumina

V4 (Vazyme, ND610) and sequenced on the DNBSEQ-T7 (MGI) platform in paired-end 150-bp mode.

CUT&Tag

CUT&Tag was performed as previously described with minor modifications[38]. Cell pellets were resuspended in NE1 buffer (20 mM HEPES-KOH, pH 7.9; 10 mM KCl; 20% glycerol; 0.01% Tween-20; 0.5 mM spermidine; 1× Roche Complete Protease Inhibitor, EDTA-free) supplemented with 0.1% NP-40 and incubated on ice for 10 min. Cells were then incubated with Concanavalin A magnetic beads (BioMag Plus, BP531B) in wash-150 buffer (20 mM HEPES, pH 7.5; 150 mM NaCl; 0.5 mM spermidine; 1× Roche Complete Protease Inhibitor, EDTA-free; 0.02% NP-40) for 10 min at room temperature with rotation. Bead-bound cells were incubated with the indicated primary and secondary antibodies in antibody buffer (wash-150 buffer supplemented with 2 mM EDTA). After washing, 1 µl pA-Tn5 (8.75 µM stock) was added and incubated with the beads in wash-300 buffer (20 mM HEPES-KOH, pH 7.5; 300 mM NaCl; 0.01% NP-40; 0.05 mM spermidine). Beads were washed several times with wash-300 buffer and resuspended in 100 µl tagmentation buffer (wash-300 buffer supplemented with 10 mM $MgCl_2$), followed by incubation at 37 °C for 1 h. Tagmentation was terminated by adding 2.5 µl 0.5 M EDTA, 2.5 µl 10% SDS, and 5 µl 10 mg/ml proteinase K (Sigma-Aldrich, R2308), followed by incubation at 55 °C for 1 h. DNA was purified by phenol–chloroform extraction and ethanol precipitation. DNA fragments were size-selected using VAHTS DNA Clean Beads (Vazyme, N411) with a two-step 0.4×/1.4× ratio purification to enrich for sequencing fragments. Sequencing libraries were prepared using the VAHTS Universal DNA Library Prep Kit for Illumina V4 (Vazyme, ND610) according to the manufacturer's instructions and sequenced on a DNBSEQ-T7 (MGI) platform in paired-end 150-bp mode (PE150).

Cell synchronization, sample collection, and cell cycle analysis

To obtain cells at different cell-cycle stages for ChEC-seq, mouse ES cells were first synchronized at M phase. Cells were treated with thymidine (2 mM; Sigma-Aldrich, T9250) for 14 h, washed twice with prewarmed DPBS, and subsequently treated with nocodazole (0.2 µg/ml; Sigma-Aldrich, M1404) for 8 h. After release, cells were collected at 1.5 h (G1 phase), 5 h (S phase), and 8 h (G2/M phase). For immunofluorescence staining, chromatin fractionation analysis, and cell-cycle progression analysis, cells were synchronized using two independent strategies. One strategy was that cells were first synchronized at M phase. Cells were treated with thymidine (2 mM) for 14 h, washed twice with prewarmed DPBS, and incubated with nocodazole for 8 h. During the final 4 h of nocodazole treatment, DMSO (Sigma, D4540) or 5-Ph-IAA (MCE, HY-134653, 1 µM) together with AGB1 (Tocris, 7686, 0.5 µM) was added. Cells were then washed three times with DPBS and released into fresh medium containing DMSO or 5-Ph-IAA plus AGB1. Samples were collected at 0, 1, 2, 3, 4, 5, 6, 7, and 8 h post-release. The other strategy is that cells were first synchronized at G1/S phase boundary. Cells were treated with thymidine (2 mM) for 14 h, washed three times with

DPBS, and released into fresh medium for 6 h. Cells were then treated with aphidicolin (2.96 μM; Aladdin, A102398) for 10 h. DMSO or 5-Ph-IAA plus AGB1 was added during the final 4 h of aphidicolin treatment. Cells were washed three times with DPBS and released into fresh medium containing DMSO or 5-Ph-IAA plus AGB1. For chromatin fractionation analysis, cells were collected at 1 h, 2 h, and 3 h after release. For cell-cycle progression analysis, cells were collected at 0 h and every hour thereafter. For DNA fiber assay and IF staining, cells were collected at 2 h after release.

For DAPI-based cell-cycle analysis, cells were fixed in ethanol and incubated in DAPI staining buffer (PBS containing 1 μg/ml DAPI (Beyotime, C1002), 100 μg/ml RNase A (Sigma-Aldrich, R6513), and 0.1% Triton X-100) at 37 °C for 30 min. Samples were stored on ice and protected from light until analysis by flow cytometry (50,000 cells per sample; Attune NxT, Thermo Fisher). Data were analyzed using FlowJo v10. For EdU incorporation assays combined with DAPI staining, cells were incubated with 20 μM EdU prior to collection and then fixed with ethanol. Fixed cells were permeabilized in DPBS containing 0.3% Triton X-100 for 10 min at room temperature and centrifuged at 1,000 × g for 3 min at 4 °C. EdU detection was performed using the BeyoClick™ EdU Cell Proliferation Kit with AF594 (Beyotime, C0079S) according to the manufacturer's instructions. Cells were subsequently incubated in DAPI staining buffer as described above and analyzed by flow cytometry (50,000 cells per sample; Attune NxT, Thermo Fisher). Data acquisition was performed using CellQuest, and flow cytometry profiles were analyzed with FlowJo v10.

Chromatin fraction analysis

Chromatin fractionation was performed as previously described with minor modifications[39]. Cells were first incubated in buffer A (10 mM HEPES, pH 7.9; 10 mM KCl; 1.5 mM $MgCl_2$; 0.34 M sucrose; 10% glycerol; 0.5 mM PMSF; 1 μg/ml aprotinin; 1 μg/ml leupeptin; 1 μg/ml pepstatin) supplemented with 0.1% Triton X-100 for 10 min at 4 °C with rotation. After centrifugation at 1,300 × g for 4 min, nuclear pellets were collected and incubated in buffer B (3 mM EDTA; 0.2 mM EGTA; 150 mM NaCl; 1 mM DTT; 1 mM PMSF; 1 μg/ml aprotinin; 1 μg/ml leupeptin; 1 μg/ml pepstatin) for 5 min on ice. Following centrifugation at 1,700 × g for 4 min, the chromatin pellets were resuspended in nuclei lysis buffer (50 mM Tris-HCl, pH 8.0; 10 mM EGTA; 1% SDS) and sonicated for 5 min (10 s on/5 s off cycles at 4 °C) using a Q800R3 sonicator. Protein concentration in the supernatant was measured using a NanoDrop spectrophotometer. Samples were mixed with 5× SDS loading buffer, boiled at 100 °C for 10 min, briefly centrifuged, and subjected to western blot analysis.

Immunofluorescence staining

Cells were fixed with 4% paraformaldehyde for 15 min at room temperature. Nuclei were extracted on ice for 5 min with 0.1% NP-40 (Diamond, A110694), washed twice with PBS, and permeabilized with 0.1% Triton X-100 for 10 min at room temperature. After two washes with PBST (0.1% Tween-

20 in PBS), cells were blocked in blocking buffer (5% BSA in PBST) for 1 h at room temperature. For primary antibody staining, cells were pelleted and resuspended in blocking buffer containing the primary antibody and incubated overnight at 4 °C. After two washes with PBST, cells were incubated with fluorophore-conjugated secondary antibodies diluted in blocking buffer for 1 h at room temperature. Following two final PBST washes, cells were mounted on coverslips (Epredia, BB1002460) using DAPI-containing mounting medium. Images were acquired using a Nikon NSPARC confocal microscope and processed with NIS-Elements AR Analysis (6.10.03).

Repli-seq

The Repli-seq experiment was performed as previously described with minor modifications[40]. Briefly, cultured cells were labeled with 100 μM BrdU (Sigma-Aldrich, 19160) for 2 h. Cells were then collected and fixed in ethanol. Fixed cells were washed with DPBS containing 1% (v/v) FBS and stained with 1 μg/ml DAPI and RNase A in PBS supplemented with 1% FBS. After incubation for 30 min at 37 °C in the dark, cells were filtered through a 40 μm nylon mesh and sorted by flow cytometry (BD FACSAria Fusion) into six fractions representing distinct stages of S phase based on DNA content. DNA from each fraction was purified by phenol–chloroform extraction followed by ethanol precipitation and sonicated to 200–500 bp fragments using a Q800R3 sonicator. DNA samples were then end-repaired, dA-tailed, and adapter-ligated using the VAHTS Universal DNA Library Prep Kit for Illumina V4 (Vazyme, ND610) according to the manufacturer's instructions. Subsequently, the adaptor-ligated DNA was denatured at 95 °C for 6 min and immediately cooled on ice. The denatured DNA was incubated with anti-BrdU antibody (BD Biosciences, 347580) and Protein G Dynabeads in IP buffer (10 mM sodium phosphate, pH 7.0; 140 mM NaCl; 0.05% Triton X-100) for 30 min at room temperature with rotation. After washing, beads were resuspended in 200 μl digestion buffer (0.5% SDS; 50 mM Tris-HCl, pH 8.0; 10 mM EDTA) and incubated at 65 °C with shaking at 900 rpm for 1 h. Eluted DNA was purified by phenol–chloroform extraction followed by ethanol precipitation. Final libraries were amplified using the VAHTS Universal DNA Library Prep Kit for Illumina V4 (Vazyme, ND610) according to the manufacturer's instructions and sequenced on a DNBSEQ-T7 (MGI) platform in paired-end 150-bp mode (PE150).

TT-seq

The TT-seq experiment was performed as previously described with minor modifications[41]. Briefly, cultured cells were labeled with 500 μM 4-thiouridine (4sU; Aladdin, T122953) for 15 min. After labeling, cells were washed twice with DPBS and lysed in TRIzol™ Reagent (Invitrogen, 15596026). Total RNA was extracted by chloroform separation followed by isopropanol precipitation. Purified RNA, together with spike-in RNA, was treated with 0.2 M NaOH on ice for 14 min, and the reaction was neutralized with 0.5 M Tris-HCl (pH 6.8). RNA was purified again by isopropanol precipitation. The recovered RNA was subjected to biotinylation in a reaction containing 10 mM HEPES-KOH, 1 mM EDTA, and 0.167 mg/ml MTSEA-biotin-XX. Biotinylated RNA was denatured at 65 °C for 5 min and immediately cooled on ice. MyOne Streptavidin C1

beads (Life Technologies, 65001) were prepared by sequential washing twice with pre-wash buffer 1 (50 mM NaCl, 0.1 M NaOH), twice with pre-wash buffer 2 (0.1 M NaCl), and twice with BW buffer (100 mM Tris-HCl, pH 7.5; 10 mM EDTA; 1 M NaCl; 0.05% Tween-20). The denatured RNA was incubated with the prepared C1 beads in BW buffer for 15 min at room temperature with rotation. Then, beads were washed four times with BW buffer at room temperature, followed by four washes with BW buffer at 65 °C with shaking at 900 rpm for 2 min each. RNA was eluted using binding buffer containing 100 mM DTT and purified with RNA Clean XP beads (Vazyme, N412). Ribosomal RNA was depleted using the Ribo-Off rRNA Depletion Kit (Human/Mouse/Rat) (Vazyme, N406-01) according to the manufacturer's instructions. RNA-seq libraries were constructed using the VAHTS Universal V10 RNA-seq Library Prep Kit (Vazyme, NR616) following the standard protocol and sequenced on a DNBSEQ-T7 (MGI) platform in paired-end 150-bp mode (PE150).

DNA fiber analysis

The DNA fiber assay was performed as previously described with minor modifications[42]. Cells were sequentially labeled with 200 μM IdU (MCE, HY-B0307) followed by 200 μM CldU (MCE, HY-112669) for 30 min each. Approximately 2,000 labeled cells were harvested and resuspended in PBS. The cell suspension was applied onto glass slides and mixed with lysis buffer (200 mM Tris-HCl pH 7.4, 50 mM EDTA, 0.5% SDS). Slides were tilted to allow DNA fibers to spread along the slide surface and air-dried. DNA fibers were fixed in methanol: acetic acid (3:1) for 15 min and denatured with 2.5 M HCl for 1 h. Slides were washed with PBS and blocked in PBS containing 1% BSA and 0.1% Triton X-100.Subsequently, the fibers were stained with primary antibodies (rat anti-BrdU for CldU detection, mouse anti-IdU, and mouse anti-ssDNA) followed by Alexa Fluor 488-(Invitrogen, A-11029), 594-(Invitrogen, A-10522), or 647(Invitrogen, A21236)-conjugated secondary antibodies. Images were acquired using an Olympus FV4000 confocal microscope. Fiber tract lengths were measured using OlyVIA software (v4.1.27564) and converted to kilobases using a conversion factor of 1 μm = 2 kb. Replication fork speed was calculated based on the length of IdU or CldU tracts and the labeling time. At least 150 DNA fibers were quantified per condition in each experiment.

Sequence data analysis

Unless otherwise stated, paired-end reads from all sequencing experiments were trimmed for adapter sequences using cutadapt v4.4[43] and aligned to the mouse reference genome (mm10) using Bowtie2 v2.5.1[44]. BAM files were processed with Picard MarkDuplicates v2.27.5 (https://broadinstitute.github.io/picard/) using default parameters to mark PCR duplicates, which were subsequently removed using samtools v1.17[45]. Unique paired-end reads were converted to bigWig format and normalized to CPM using deepTools v3.5.2[46].

ChOR-seq and TT-seq data processing

ChOR-seq reads were processed according to the sequencing data preprocessing workflow, with Drosophila melanogaster (dm6) spike-in reads included as an internal control. CPM normalized bigWig files were generated using deepTools v3.5.2[46] and further corrected based on spike-in normalization.

TT-seq reads were trimmed with Trim Galore v0.6.10 (https://www.bioinformatics.babraham.ac.uk/projects/trim_galore/) and aligned to mm10 using STAR v2.7.10b[47], with Drosophila melanogaster (dm6) spike-in reads included. BAM files were deduplicated using Picard MarkDuplicates v2.27.5 (https://broadinstitute.github.io/picard/) and filtered for uniquely mapped reads using samtools v1.17[45]. BigWig files were generated using deepTools v3.5.2, normalized to RPKM, and corrected using spike-in controls[46].

Peak calling and statistical analysis

Peaks from ChIP-seq and ChEC-seq datasets were called using MACS2 v2.2.7.1[48]. Peaks overlapping ENCODE blacklist regions were removed using BEDTools v2.31.0[49]. Peak annotation was performed with homer v4.11.1 (annotatePeaks.pl) [50], incorporating repeat annotations from the UCSC Genome Browser to classify repetitive elements.

Comparisons of signal intensities between groups were performed using the Wilcoxon signed-rank test. Peak overlaps among different omics datasets were determined using BEDTools v2.31.0 [49], and tag density heatmaps centered on enriched region were generated using deepTools v3.5.2 [46] Genome-wide tracks were visualized using IGV (Integrative Genomics Viewer) [51].

ORC1 clustering

Signal intensities for ATAC-seq and ChIP-seq datasets (H3K4me3, H3K9ac, H3K27ac, H3K4me1, H3K9me3, and H3K27me3) were quantified across ORC1 peak regions. A multi-omics signal matrix was constructed, and the signal values for each peak were normalized by row-wise Z-score transformation. The normalized matrix was visualized using the R package *pheatmap*, with Pearson correlation as the distance metric and hierarchical clustering performed using the Ward.D2 method.

Repli-ChEC data analysis

Repli-ChEC reads were processed using the general sequencing data preprocessing workflow, with Drosophila melanogaster (dm6) spike-in reads included as an internal control. Downstream analysis was performed as previously described by Flury et al.[28]. Using the EdU-purified Input samples ('ClickedInputs') as a reference for relative spike-in abundance and EdU labeling efficiency, the downsampling factor was calculated as:

$$Downsampling\ factor = \alpha \cdot \frac{1}{Repli-ChEC\ dm6\ reads} \cdot \frac{ClickedInput\ (dm6\ reads)}{ClickedInput\ (mm10\ reads)}$$

Here, α represents a normalization coefficient, with the maximum downsampling factor set to 1 and the remaining factors scaled proportionally. BigWig files were generated using deepTools v3.5.2, normalized to CPM, and adjusted according to the calculated downsampling factor for downstream analyses[46].

ORC1 signal intensities were quantified across all peaks, and only changes occurring within 2 hours were included in the signal recovery analysis. Peaks were classified as “restored” if the signal at a later time point T(X+n) did not exceed 1.5-fold of R(X) (T(X+n)/R(X) < 1.5, and as “unstable” if the signal decreased by more than 1.5-fold.

ORC1 signal recovery curves were plotted in R v4.2.3[52] and fitted using a first order equation:

$$y = y_{\max} - b \cdot e^{(-k \cdot t)}$$

In this equation, y_{max} represents the maximum level of the evaluated ORC1 signal, t is time, k is the kinetic parameter, and b is a labeling-specific parameter describing the relative change from the initial signal to the saturated signal.

Data availability

High throughput sequencing data generated in this study are being deposited to Gene Expression Omnibus (GEO) database (https://www.ncbi.nlm.nih.gov/geo/). Publicly available datasets analyzed in this study were obtained from the following sources: Free MNase data (GEO: GSM7779149, MNase 10 min) were used as a control dataset for the ChEC-seq experiments. SNS-seq bigWig and peak files were retrieved from GEO under accession GSM2651112. OK-seq data, including bigWig files containing smoothed partition and replication fork directionality (RFD) scores, alongside text files with 1-kb resolution coordinates of initiation zones (IZs), were downloaded from GEO under accession GSM3290342. For downstream analyses, these IZ regions were further extended to 100 kb. Mouse embryonic stem cell (mESC) ERCEs were acquired from GEO under accession GSE114139. ChIP-seq BAM files for H3K4me3, H3K9ac, H3K27ac, H3K4me1, H3K9me3, and H3K27me3 in mouse ES cell line Bruce4 were downloaded from the ENCODE portal (https://www.encodeproject.org; accession: ENCSR343RKY) and merged for peak calling. All other data are available from the corresponding author upon reasonable request.

Acknowledgments

This work was supported by the National Nature Science Foundation of China (32422015, 32370647), the Shenzhen Science and Technology Program grant (RCYX20221008092930079), the Ministry of Science and Technology of China (2022YFA1302801), the Shenzhen Medical Research Fund (B2402044) to H.L., the National Natural Science Foundation of China (32521002) to H.L and H.Z., the National Natural Science Foundation of China (32570702) and the Guangdong Basic and Applied Basic Research Foundation (2026A1515011436)to Z.W., and the Fundamental Research Program of Shanxi Province (202203021212515) to R.Z. We thank Yisui Xia for critical reading and discussion of the manuscript. The Biochemical Analysis Core of Shenzhen Bay Laboratory, and the Biomedical Imaging Core Facility at the Bio-Tech Center of Shenzhen Medical Academy of Research and Translation (SMART) provided technical assistance.

Author contributions

R.Z. generated knock-in cell lines, conducted majority experiments, and composed the figures. X.Z performed bioinformatics of next-generation sequencing data analysis and composed the figures. N.W collected the materials, performed seq and biochemical experiments. W.G. performed DNA fiber analysis and assisted in seq experiments. M.C assisted in seq experiments and biochemical analysis. X.B. and H.Z. helped to discuss the project. Z.W. and H.L. designed and supervised the project, analyzed the data and wrote the manuscript.

Competing interests

The authors declare no competing interests.

References

1 Stillman, B., Diffley, J. F. X. & Iwasa, J. H. Mechanisms for licensing origins of DNA replication in eukaryotic cells. *Nature Structural & Molecular Biology* **32**, 1143-1153, doi:10.1038/s41594-025-01587-5 (2025).

2 Dhar, M. K., Sehgal, S. & Kaul, S. Structure, replication efficiency and fragility of yeast ARS elements. *Research in Microbiology* **163**, 243-253, doi:http://dx.doi.org/10.1016/j.resmic.2012.03.003 (2012).

3 Hu, Y. & Stillman, B. Origins of DNA replication in eukaryotes. *Mol Cell* **83**, 352-372, doi:10.1016/j.molcel.2022.12.024 (2023).

4 Vashee, S., Simancek, P., Challberg, M. D. & Kelly, T. J. Assembly of the Human Origin Recognition Complex*. *Journal of Biological Chemistry* **276**, 26666-26673, doi:https://doi.org/10.1074/jbc.M102493200 (2001).

5 Kuo, A. J. *et al.* The BAH domain of ORC1 links H4K20me2 to DNA replication licensing and Meier-Gorlin syndrome. *Nature* **484**, 115-119, doi:http://www.nature.com/nature/journal/v484/n7392/abs/nature10956.html#supplementary-information (2012).

6 Jaremko, M. J., On, K. F., Thomas, D. R., Stillman, B. & Joshua-Tor, L. The dynamic nature of the human origin recognition complex revealed through five cryoEM structures. *eLife* **9**, e58622, doi:10.7554/eLife.58622 (2020).

7 Kara, N., Hossain, M., Prasanth, S. G. & Stillman, B. Orc1 Binding to Mitotic Chromosomes Precedes Spatial Patterning during G1 Phase and Assembly of the Origin Recognition Complex in Human Cells*. *Journal of Biological Chemistry* **290**, 12355-12369, doi:https://doi.org/10.1074/jbc.M114.625012 (2015).

8 Tatsumi, Y., Ohta, S., Kimura, H., Tsurimoto, T. & Obuse, C. The ORC1 Cycle in Human Cells: I. CELL CYCLE-REGULATED OSCILLATION OF HUMAN ORC1. *Journal of Biological Chemistry* **278**, 41528-41534, doi:10.1074/jbc.M307534200 (2003).

9 Ohta, S., Tatsumi, Y., Fujita, M., Tsurimoto, T. & Obuse, C. The ORC1 Cycle in Human Cells: II. DYNAMIC CHANGES IN THE HUMAN ORC COMPLEX DURING THE CELL CYCLE. *Journal of Biological Chemistry* **278**, 41535-41540, doi:10.1074/jbc.M307535200 (2003).

10 Hossain, M., Bhalla, K. & Stillman, B. Multiple, short protein binding motifs in ORC1 and CDC6 control the initiation of DNA replication. *Mol Cell* **81**, 1951-1969.e1956, doi:10.1016/j.molcel.2021.03.003 (2021).

11 Vermeulen, M. *et al.* Quantitative interaction proteomics and genome-wide profiling of epigenetic histone marks and their readers. *Cell* **142**, 967-980, doi:10.1016/j.cell.2010.08.020 (2010).

12 Prasanth, S. G., Shen, Z., Prasanth, K. V. & Stillman, B. Human origin recognition complex is essential for HP1 binding to chromatin and heterochromatin organization. *Proceedings of the National Academy of Sciences of the United States of America* **107**, 15093-15098, doi:10.1073/pnas.1009945107 (2010).

13 Hossain, M. & Stillman, B. Opposing roles for DNA replication initiator proteins ORC1 and CDC6 in control of Cyclin E gene transcription. *Elife* **5**, doi:10.7554/eLife.12785 (2016).

14 Hemerly, A. S., Prasanth, S. G., Siddiqui, K. & Stillman, B. Orc1 Controls Centriole and Centrosome Copy Number in Human Cells. *Science* **323**, 789-793, doi:10.1126/science.1166745 (2009).

15 Li, S. *et al.* Origin recognition complex harbors an intrinsic nucleosome remodeling activity. *Proceedings of the National Academy of Sciences of the United States of America* **119**, e2211568119, doi:10.1073/pnas.2211568119 (2022).

16 Chacin, E. *et al.* Establishment and function of chromatin organization at replication origins. *Nature* **616**, 836-842, doi:10.1038/s41586-023-05926-8 (2023).

17 Zhou, M. *et al.* ORC1 enhances repressive epigenetic modifications on HIV-1 LTR to promote HIV-1 latency. *J Virol* **98**, e0003524, doi:10.1128/jvi.00035-24 (2024).

18 Dellino, G. I. *et al.* Genome-wide mapping of human DNA-replication origins: levels of transcription at ORC1 sites regulate origin selection and replication timing. *Genome Res* **23**, 1-11, doi:10.1101/gr.142331.112 (2013).

19 Long, H. *et al.* H2A.Z facilitates licensing and activation of early replication origins. *Nature* **577**, 576-581, doi:10.1038/s41586-019-1877-9 (2020).

20 Su, Z. *et al.* Regulation of epigenetics and chromosome structure by human ORC2. *Cell Reports* **44**, doi:10.1016/j.celrep.2025.115816 (2025).

21 Zentner, G. E., Kasinathan, S., Xin, B., Rohs, R. & Henikoff, S. ChEC-seq kinetics discriminates transcription factor binding sites by DNA sequence and shape in vivo. *Nat Commun* **6**, 8733, doi:10.1038/ncomms9733 (2015).

22 Almeida, R. *et al.* Chromatin conformation regulates the coordination between DNA replication and transcription. *Nat Commun* **9**, 1590, doi:10.1038/s41467-018-03539-8 (2018).

23 Petryk, N. *et al.* MCM2 promotes symmetric inheritance of modified histones during DNA replication. *Science* **361**, 1389-1392, doi:10.1126/science.aau0294 (2018).

24 Sima, J. *et al.* Identifying cis Elements for Spatiotemporal Control of Mammalian DNA Replication. *Cell* **176**, 816-830.e818, doi:10.1016/j.cell.2018.11.036 (2019).

25 Bechhoefer, J. & Rhind, N. Replication timing and its emergence from stochastic processes. *Trends Genet* **28**, 374-381, doi:10.1016/j.tig.2012.03.011 (2012).

26 Nakatani, T. Dynamics of replication timing during mammalian development. *Trends Genet* **41**, 568-576, doi:10.1016/j.tig.2025.01.010 (2025).

27 Hiraga, S. I. *et al.* Human RIF1 and protein phosphatase 1 stimulate DNA replication origin licensing but suppress origin activation. *EMBO Rep* **18**, 403-419, doi:10.15252/embr.201641983 (2017).

28 Flury, V. *et al.* Recycling of modified H2A-H2B provides short-term memory of chromatin states. *Cell* **186**, 1050-1065.e1019, doi:10.1016/j.cell.2023.01.007 (2023).

29 Hatoyama, Y. *et al.* Combination of AID2 and BromoTag expands the utility of degron-based protein knockdowns. *EMBO Rep* **25**, 4062-4077, doi:10.1038/s44319-024-00224-4 (2024).

30 Fragkos, M., Ganier, O., Coulombe, P. & Mechali, M. DNA replication origin activation in space and time. *Nat Rev Mol Cell Biol* **16**, 360-374, doi:10.1038/nrm4002 (2015).

31 Matsui, T. *et al.* Proviral silencing in embryonic stem cells requires the histone methyltransferase ESET. *Nature* **464**, 927-931, doi:10.1038/nature08858 (2010).

32 Lu, X. Regulation of endogenous retroviruses in murine embryonic stem cells and early embryos. *J Mol Cell Biol* **15**, doi:10.1093/jmcb/mjad052 (2024).

33 Miotto, B., Ji, Z. & Struhl, K. Selectivity of ORC binding sites and the relation to replication timing, fragile sites, and deletions in cancers. *Proceedings of the National Academy of Sciences of the United States of America* **113**, E4810-4819, doi:10.1073/pnas.1609060113 (2016).

34 Reuter, L. M. *et al.* MCM2-7 loading-dependent ORC release ensures genome-wide origin licensing. *Nature Communications* **15**, 7306, doi:10.1038/s41467-024-51538-9 (2024).

35 Wen, Z. *et al.* Nucleosome wrapping states encode principles of 3D genome organization. *Nat Commun* **16**, 352, doi:10.1038/s41467-024-54735-8 (2025).

36 Liu, C. *et al.* Histone H1 facilitates restoration of H3K27me3 during DNA replication by chromatin compaction. *Nature Communications* **14**, 4081, doi:10.1038/s41467-023-39846-y (2023).

37 Petryk, N. *et al.* Genome-wide and sister chromatid-resolved profiling of protein occupancy in replicated

chromatin with ChOR-seq and SCAR-seq. *Nature Protocols* **16**, 4446-4493, doi:10.1038/s41596-021-00585-3 (2021).

38 Kaya-Okur, H. S. *et al.* CUT&Tag for efficient epigenomic profiling of small samples and single cells. *Nature Communications* **10**, 1930, doi:10.1038/s41467-019-09982-5 (2019).

39 Méndez, J. & Stillman, B. Chromatin association of human origin recognition complex, cdc6, and minichromosome maintenance proteins during the cell cycle: assembly of prereplication complexes in late mitosis. *Mol Cell Biol* **20**, 8602-8612, doi:10.1128/mcb.20.22.8602-8612.2000 (2000).

40 Marchal, C. *et al.* Genome-wide analysis of replication timing by next-generation sequencing with E/L Repli-seq. *Nature Protocols* **13**, 819-839, doi:10.1038/nprot.2017.148 (2018).

41 Gregersen, L. H., Mitter, R. & Svejstrup, J. Q. Using TT(chem)-seq for profiling nascent transcription and measuring transcript elongation. *Nat Protoc* **15**, 604-627, doi:10.1038/s41596-019-0262-3 (2020).

42 Nakamura, K. *et al.* Proteome dynamics at broken replication forks reveal a distinct ATM-directed repair response suppressing DNA double-strand break ubiquitination. *Mol Cell* **81**, 1084-1099.e1086, doi:10.1016/j.molcel.2020.12.025 (2021).

43 Martin, M. CUTADAPT removes adapter sequences from high-throughput sequencing reads. *EMBnet.journal* **17**, doi:10.14806/ej.17.1.200 (2011).

44 Langmead, B., Trapnell, C., Pop, M. & Salzberg, S. L. Ultrafast and memory-efficient alignment of short DNA sequences to the human genome. *Genome Biol* **10**, R25, doi:10.1186/gb-2009-10-3-r25 (2009).

45 Li, H. *et al.* The Sequence Alignment/Map format and SAMtools. *Bioinformatics* **25**, 2078-2079, doi:10.1093/bioinformatics/btp352 (2009).

46 Ramírez, F. *et al.* deepTools2: a next generation web server for deep-sequencing data analysis. *Nucleic Acids Res* **44**, W160-165, doi:10.1093/nar/gkw257 (2016).

47 Dobin, A. *et al.* STAR: ultrafast universal RNA-seq aligner. *Bioinformatics* **29**, 15-21, doi:10.1093/bioinformatics/bts635 (2013).

48 Zhang, Y. *et al.* Model-based analysis of ChIP-Seq (MACS). *Genome Biol* **9**, R137, doi:10.1186/gb-2008-9-9-r137 (2008).

49 Quinlan, A. R. & Hall, I. M. BEDTools: a flexible suite of utilities for comparing genomic features. *Bioinformatics* **26**, 841-842, doi:10.1093/bioinformatics/btq033 (2010).

50 Heinz, S. *et al.* Simple combinations of lineage-determining transcription factors prime cis-regulatory elements required for macrophage and B cell identities. *Mol Cell* **38**, 576-589, doi:10.1016/j.molcel.2010.05.004 (2010).

51 Robinson, J. T. *et al.* Integrative genomics viewer. *Nat Biotechnol* **29**, 24-26, doi:10.1038/nbt.1754 (2011).

52 Team, R. A language and environment for statistical computing. *Computing* **1**, doi:10.1890/0012-9658(2002)083[3097:CFHIWS]2.0.CO;2 (2006).

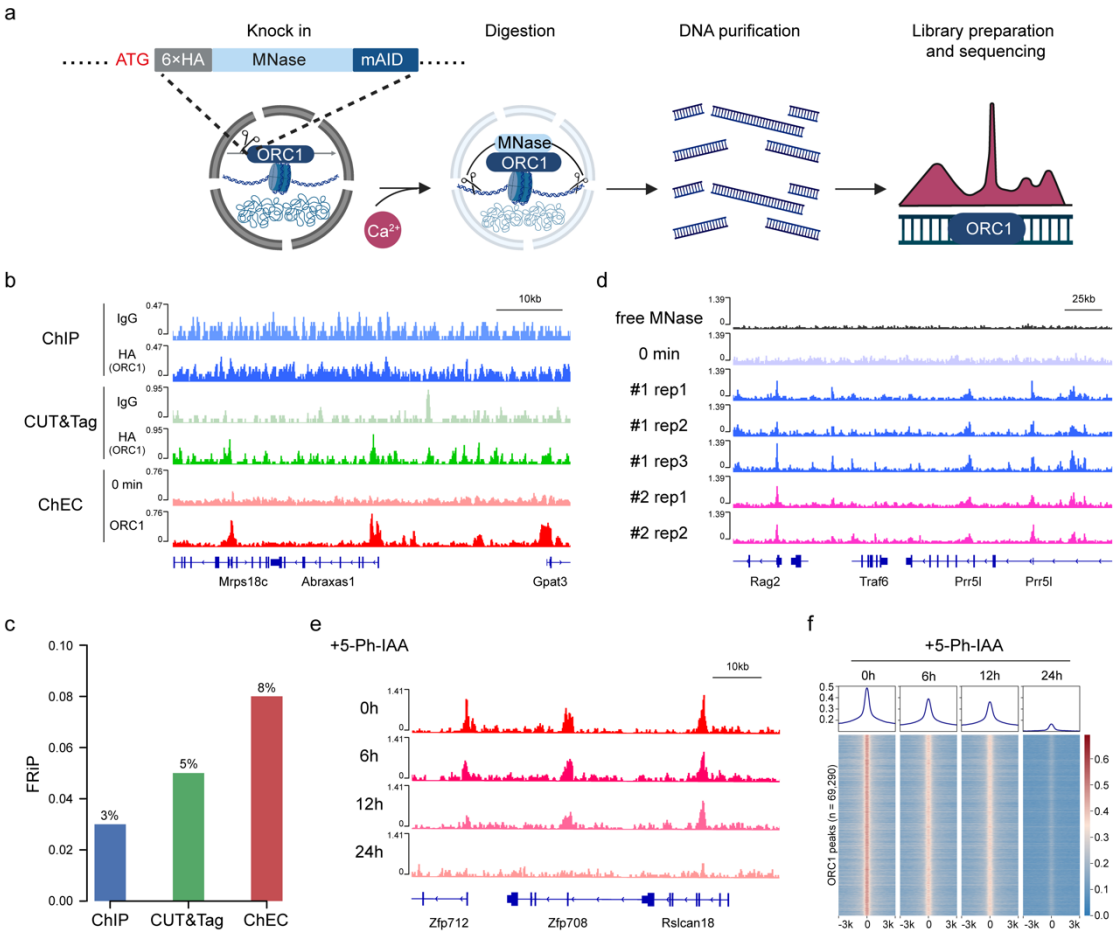

Figure 1. ChEC-seq maps endogenous ORC1 binding with high specificity and robustness.

a. Diagram shows the construction of 6×HA-MNase-mAID-ORC knock-in cell line and ChEC-seq procedure.

b. IGV snapshot shows that ORC1 ChEC-seq has higher signal-to-noise ratio compared to ChIP-seq or CUT&Tag by HA antibody.

c. Bar plot shows the FRiP (Fraction of Reads in Peaks) of ORC1 ChIP-seq, CUT&Tag and ChEC-seq within ORC1 ChEC peaks (n = 69,290).

d. IGV snapshot shows that ORC1 ChEC-seq signal is specific compared with free MNase and 0-min sample, and stable between replicates and different clones.

e. IGV snapshot shows the distribution of ORC1 ChEC signal during 5-Ph-IAA induced ORC1 degradation.

f. Heatmaps show the genome-wide dynamics of ORC1 ChEC signal during 5-Ph-IAA induced ORC1 degradation.

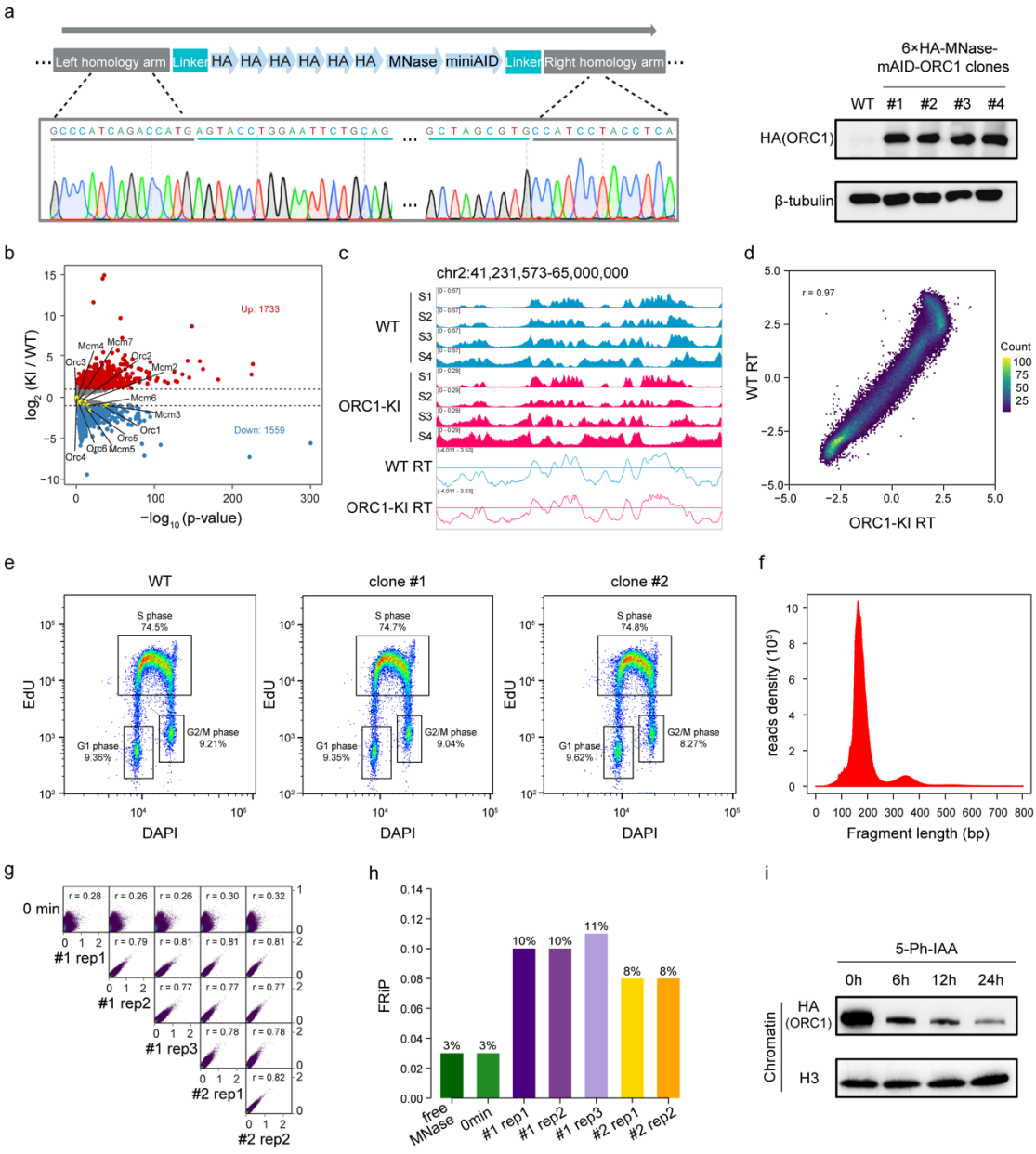

Extended Figure 1. Different 6×HA-MNase-mAID-ORC1 clones exhibit high reproducibility and strong quantitative correlations.

a. Genotyping and western blot results verify the successful construction of 6×HA-MNase-mAID-ORC1 knock-in cell lines.

b. Volcano plot shows genome-wide expression dynamics in wild type (WT) and 6×HA-MNase-mAID-ORC1 knock-in mouse ES cells; Genes with a $|\log_2(KI/WT)| > 1$ and P-values < 0.05 were selected as differentially expressed genes.

c. IGV snapshot shows the BrdU signal of S1~S4 fractions and replication timing of WT and 6×HA-MNase-mAID-ORC1 knock-in mouse ES cells.

d. Dot plots show the genome-wide correlation of replication timing between WT and 6×HA-MNase-mAID-ORC1 knock-in mouse ES cells.

e. FACS analysis of the cell cycle distribution of WT and 6×HA-MNase-mAID-ORC1 knock-in mouse ES cells.

f. Histogram shows the enrichment of characteristic mono-nucleosome fragments during ORC1 ChEC-seq.

g. Dot plots show the correlation among input and ORC1 ChEC replicates and clones, calculated using genome-wide 1 kb bins.

h. Bar plot shows the FRiP of ORC1 ChEC signal in control samples (free MNase and 0 min), technical replicates, and different knock-in clones within ORC1 ChEC peaks (n = 69,290).

i. Western blot analysis shows the levels of chromatin bound HA-ORC1 at different 5-Ph-IAA treatment times.

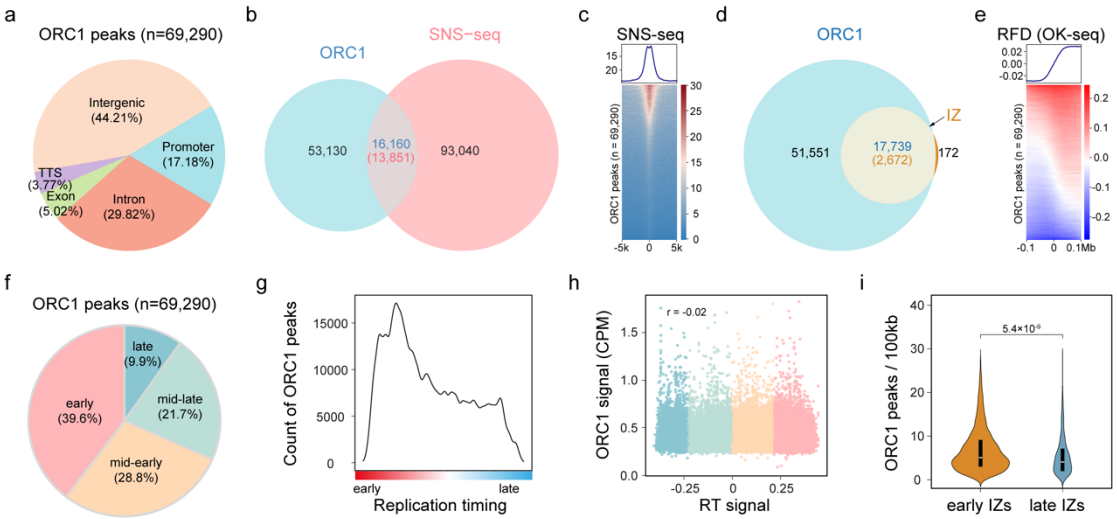

Figure 2. ORC1 binding density, rather than individual peak intensity, correlates with replication timing.

a. Genome-wide distribution of ORC1 ChEC peaks.

b. Venn diagram shows the overlap between ORC1 ChEC peaks (n = 69,290) and short nascent strand sequencing (SNS-seq) peaks (n = 106,891).

c. Heatmap shows the distribution of SNS-seq (n= 106,891) around ORC1 ChEC peaks (n = 69,290).

d. Venn diagram shows the overlap between OK-seq-derived initiation zones (IZs, n = 2,844, each 100 kb in length) and ORC1 ChEC peaks.

e. Heatmap shows the distribution of OK-seq replication fork directionality (RFD) signal around ORC1 ChEC peaks (n = 69,290).

f. Genome-wide distribution of ORC1 ChEC peaks in four replication timing categories.

g. Density plot shows the count of ORC1 peaks across replication timing regions.

h. Dot plot shows the correlation between ORC1 signals and replication timing signals in ORC1 peak regions (n = 69,290).

i. Violin plot shows ORC1 peak counts per 100kb region for early (n = 2,171) and late (n = 673) initiation zones (IZs, each 100 kb in length).

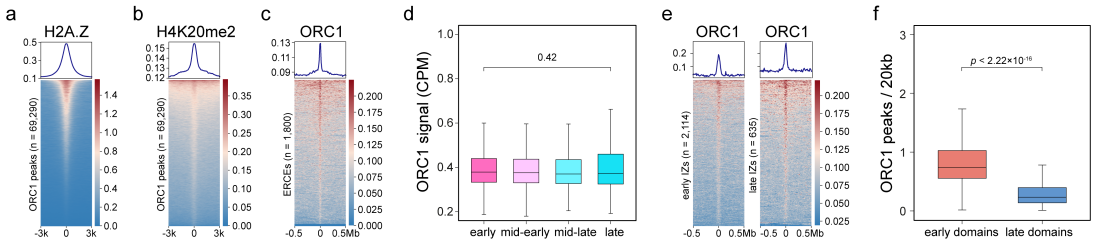

924

925 **Extended Figure 2. The correlation of ORC1 ChEC peaks with replication timing and their co-localization**
926 **with H2A.Z and H4K20me2 across the genome.**

927 a. Heatmap shows the distribution of H2A.Z around ORC1 ChEC peaks (n = 69,290).

928 b. Heatmap shows the distribution of H4K20me2 around ORC1 ChEC peaks (n = 69,290).

929 c. Heatmap shows the distribution of ORC1 signals in the ERCE regions (n =1,800).

930 d. Box plot shows the signals of ORC1 in different RT categories.

931 e. Heatmap shows the distribution of ORC1 signals in early IZs (n =2,114) and late IZs (n = 635).

932 f. Box plot shows ORC1 peak counts per 20kb region in early RT domains (n = 628) and late RT domains (n = 608).

933

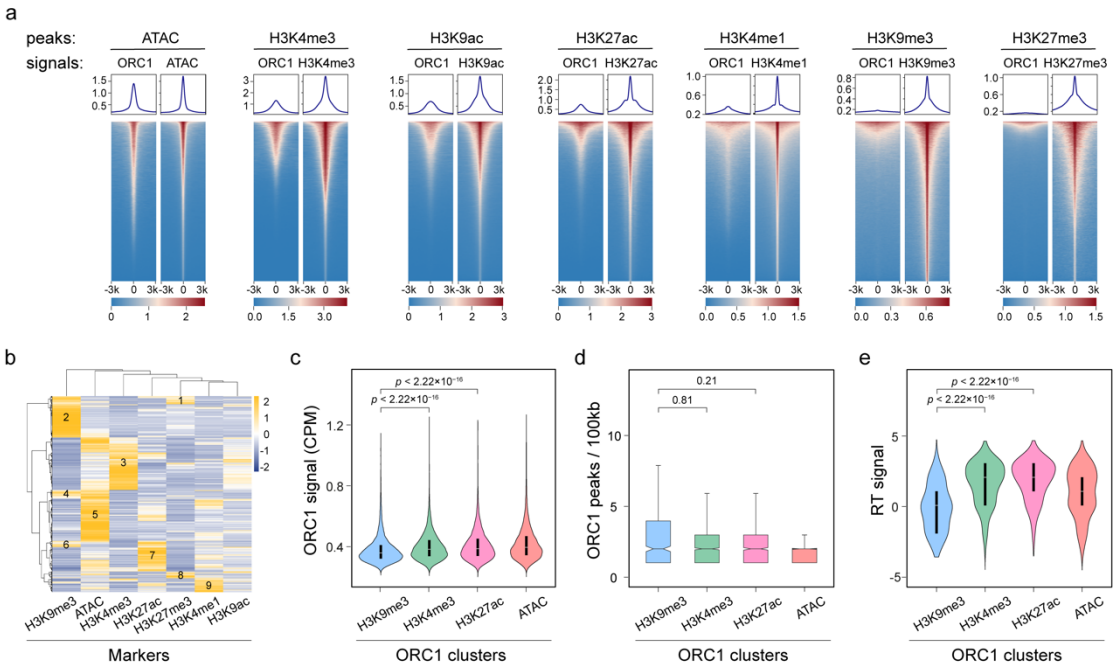

Figure 3. ORC1 occupies both euchromatic and heterochromatic domains with distinct replication timing profiles.

a. Heatmaps show the distribution of ORC1 signals within peaks of ATAC (n = 128,248), H3K4me3 (n = 63,563), H3K9ac (n = 77,740), H3K27ac (n = 59,890), H3K4me1 (n = 190,225), H3K27me3 (n = 8,034) and H3K9me3 (n = 51,022).

b. Heatmap shows the clustering of ORC1 ChEC peaks (n = 65,000) based on epigenetic states. Each column represents the distribution of an epigenetic factor across ORC1 regions. Yellow indicates high signal; blue indicates low signal.

c. Violin plot shows ORC1 signals across ORC1 clusters associated with H3K9me3 (n = 10,963), H3K4me3 (n = 17,459), H3K27ac (n = 8,084), and ATAC (n = 13,900).

d. Box plot shows ORC1 peak counts per 100 kb region across ORC1 clusters within initiation zones (IZs, n = 2,844, each 100 kb in length).

e. Violin plot shows the RT signals in different ORC1 clusters.

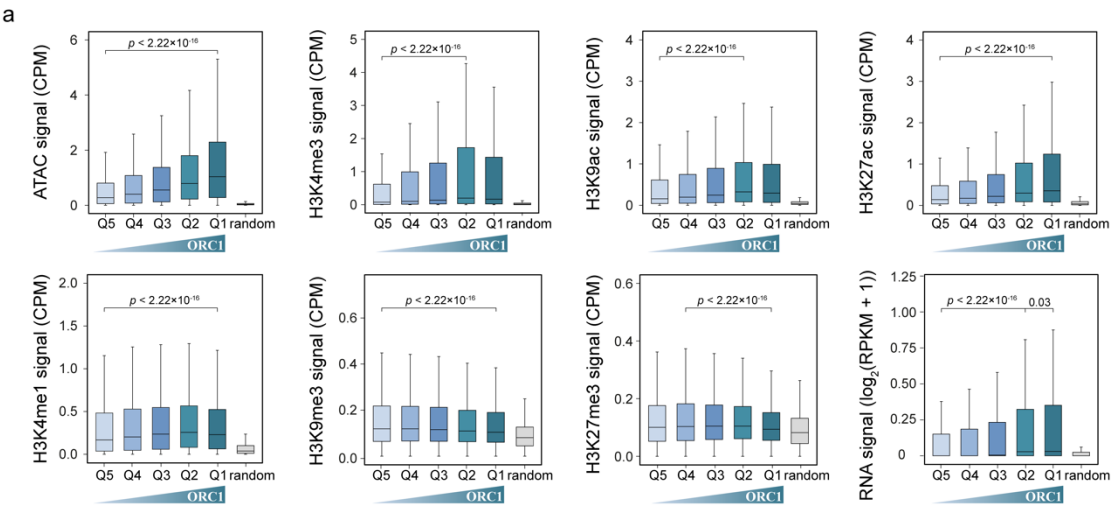

Extended Figure 3. ORC1 signal intensity correlates with euchromatic features but shows no correlation with H3K4me1, H3K9me3, or H3K27me3.

a. Box plots show the signals of ATAC, H3K4me3, H3K9ac, H3K27ac, H3K4me1, H3K9me3, H3K27me3 and RNA-seq in different ORC1 peak regions (Q1-Q5). Q1-Q5 are clustered according to ORC1 signals. Q1 indicates high signal; Q5 indicates low signal.

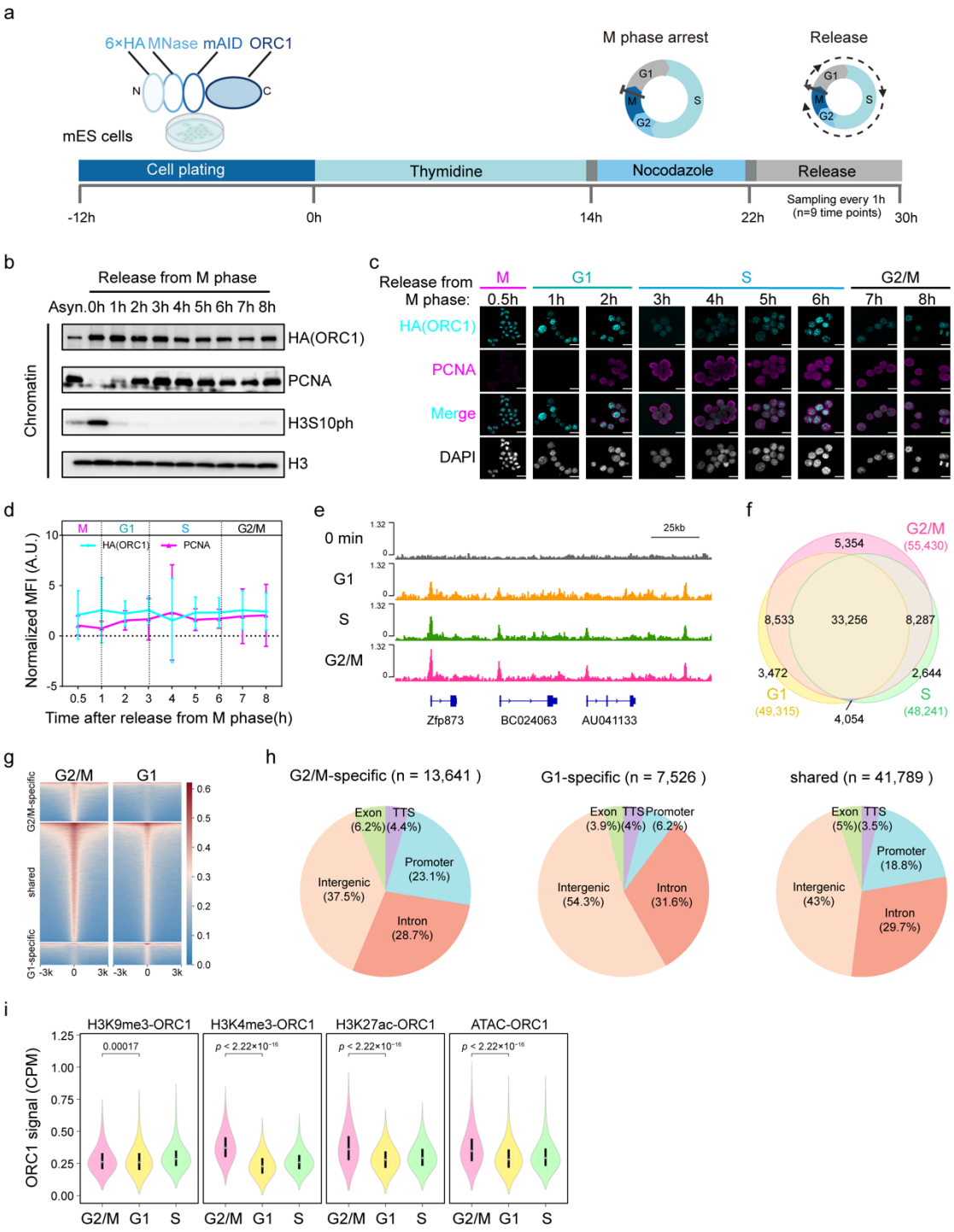

Figure 4. Cell cycle profiling of ORC1 reveals continuous chromatin association and G2/M-to-G1 spatial redistribution.

a. Diagram shows the strategy of cell cycle synchronization and release.

b. Western blot shows the levels of chromatin-bound HA-ORC1 at different time points after releasing from M phase. Asyn., asynchronous cells.

c. IF staining detecting the distribution of HA-ORC1 (cyan) and PCNA (magenta) across cell cycle, with DAPI (white) as a nuclear counterstain. Scale bar, 25 μm.

d. The statistical analysis of Fig. 4c. The X-axis represents time points (hours) after release from M phase. The Y-axis represents the normalized mean fluorescence intensity (MFI) of the nuclei per cell (n = 150 cells). Data are presented as mean ± SD.

e. IGV snapshot shows the signals of ORC1 ChEC data in G1, S and G2/M phases.

f. Venn diagram shows the overlap of ORC1 peaks in G1 (n = 49,315), S (n = 48,241) and G2/M (n = 55,430) phases.

g. Heatmaps shows ORC1 signals in G1 and G2/M phases across G2/M-specific (n = 13,641), shared (n = 41,789), and G1-specific (n = 7,526) regions. G2/M-specific regions are defined as those in which ORC1 signals decrease markedly from G2/M to G1, whereas G1-specific regions are those in which ORC1 signals increase markedly from G2/M to G1. All remaining regions are classified as shared.

h. Genome-wide distributions of ORC1 peaks in G2/M-specific, G1-specific and shared regions.

i. Violin plots show ORC1 signals across ORC1 clusters associated with H3K9me3 (n = 10,963), H3K4me3 (n = 17,459), H3K27ac (n = 8,084), and ATAC (n = 13,900), throughout the cell cycle.

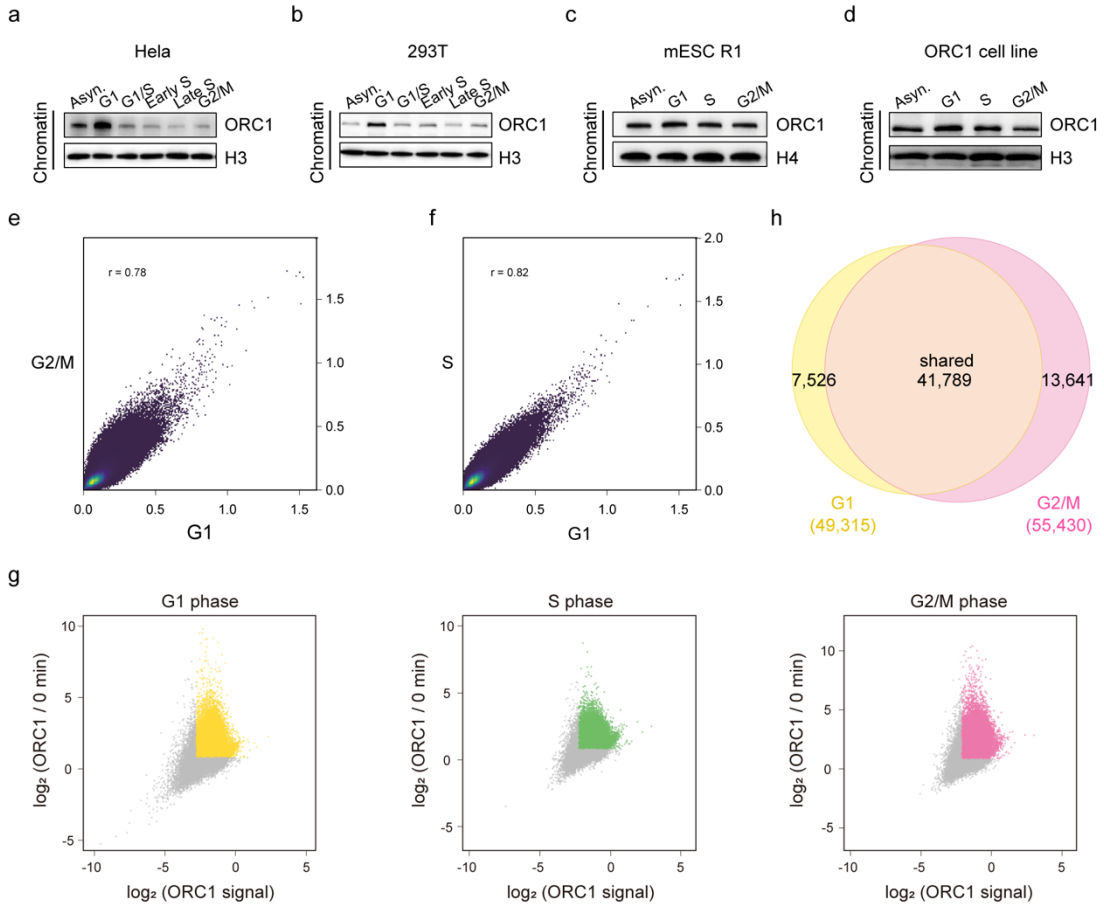

Extended Figure 4. The global ORC1 binding landscape is largely maintained throughout the mES cell cycle.

a-b. Western blot analysis shows the levels of chromatin-bound ORC1 across different cell-cycle phases in HeLa cells (a) and 293T cells (b).

c-d. Western blot analysis shows the levels of chromatin-bound ORC1 across different cell-cycle phases in wild-type mouse ES cells (c) and ORC1 knock-in cells (d).

e. Dot plot shows the correlation between G1 and G2/M ORC1 signals in total ORC1 peak regions (n = 69,290).

f. Dot plot shows the correlation between G1 and S ORC1 signals in total ORC1 peak regions (n = 69,290).

g. Yellow, green, and purple indicate high-confidence ORC1 peaks in G1, S, and G2/M phases, respectively. The X-axis represents $\log_2$ ORC1 signals of each phase in total ORC1 peak regions (lowest 10% of signals excluded). The Y-axis represents $\log_2$ fold change between cleavage-treated and 0-min control samples for each phase; peaks with $\log_2$ fold change > 0.8 were selected.

h. Venn diagram shows the overlap between ORC1 peaks in G1 (n = 49,315) and G2/M (n = 55,430) phases.

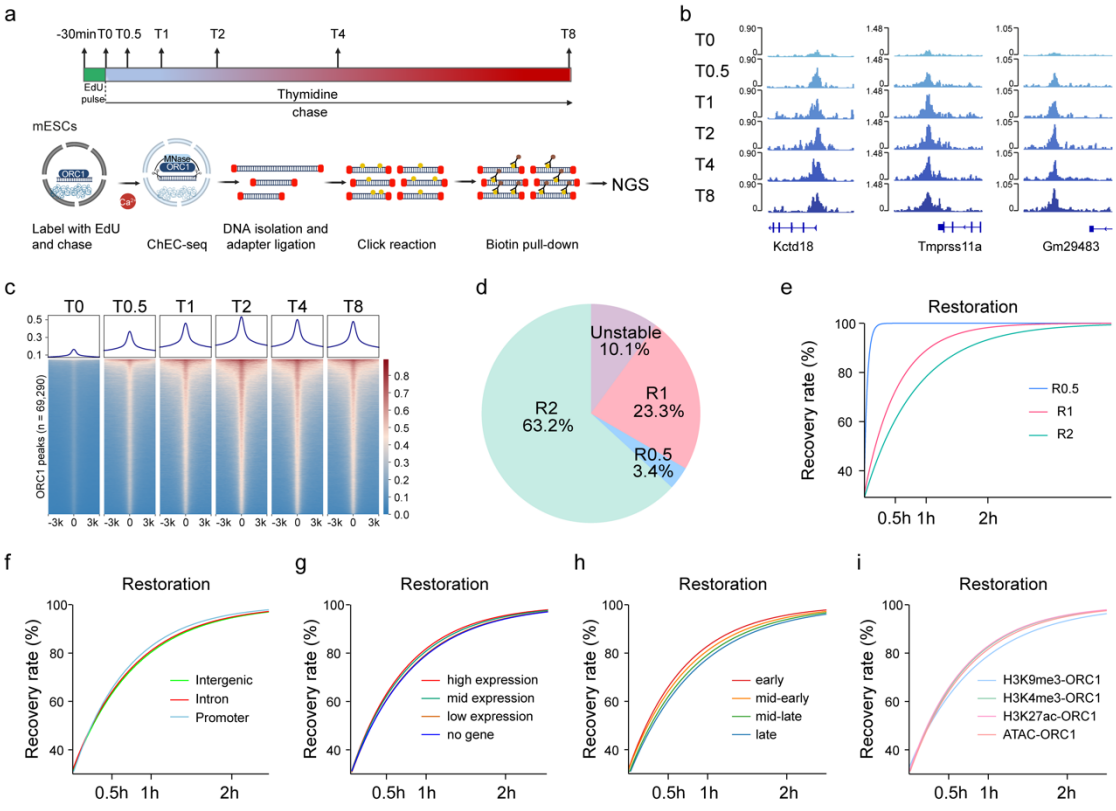

Figure 5. ORC1 recovers chromatin binding rapidly after DNA replication.

a. Schematic diagram of repli-ChEC-seq workflow. KI mouse ES cells were pulse-labeled with EdU for 30 min. Nascent chromatin was harvested immediately after EdU labeling (T0). Mature chromatin was collected at different time points (T0.5, T1, T2, T4 and T6 hours) following thymidine chase after EdU labeling.

b-c. IGV snapshots (b) and heatmaps (c) show the distribution of ORC1 in different chasing time points.

d. Pie chart shows the proportions of four recovery categories of ORC1 peaks. R0.5, R1, and R2 indicate peaks restored at 0.5 h, 1 h, and 2 h, respectively. “Unstable” indicates peaks whose signals do not increase consistently during the chase.

e. Curves show the recovery rates of three recovery categories of ORC1 peaks.

f-i. Curves show the recovery rates of ORC1 peaks across different genomic regions (f), genes (g), replication timing (h), and epigenetic states (i).

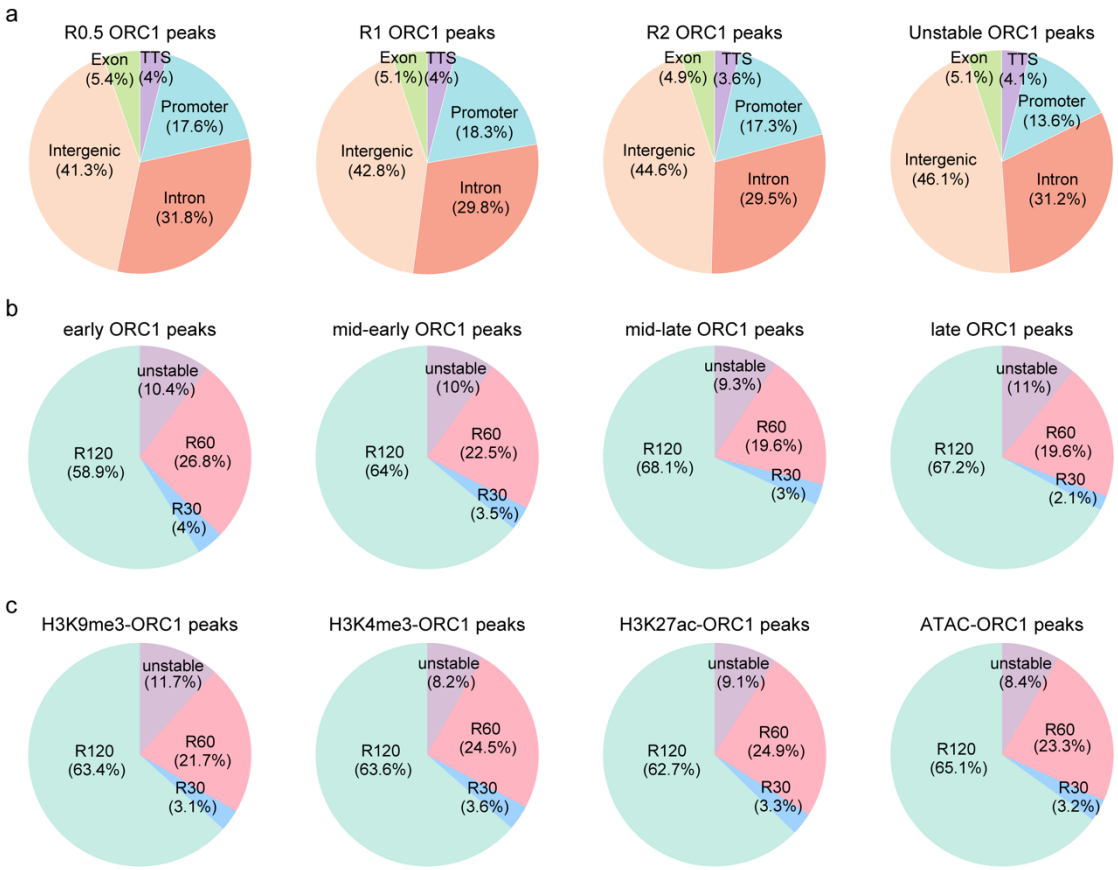

Extended Figure 5. ORC1 rapidly recovers after replication, and its recovery is largely independent of local genomic distribution, transcriptional activity, replication timing, and epigenetic states.

a. Pie charts show the genome-wide distribution of the four categories of ORC1 peaks.

b. Pie charts show the proportions of ORC1 peaks with different recovery rates across early, mid-early, mid-late and late replication timing regions.

c. Pie charts show the proportions of recovery categories rates across ORC1 clusters.

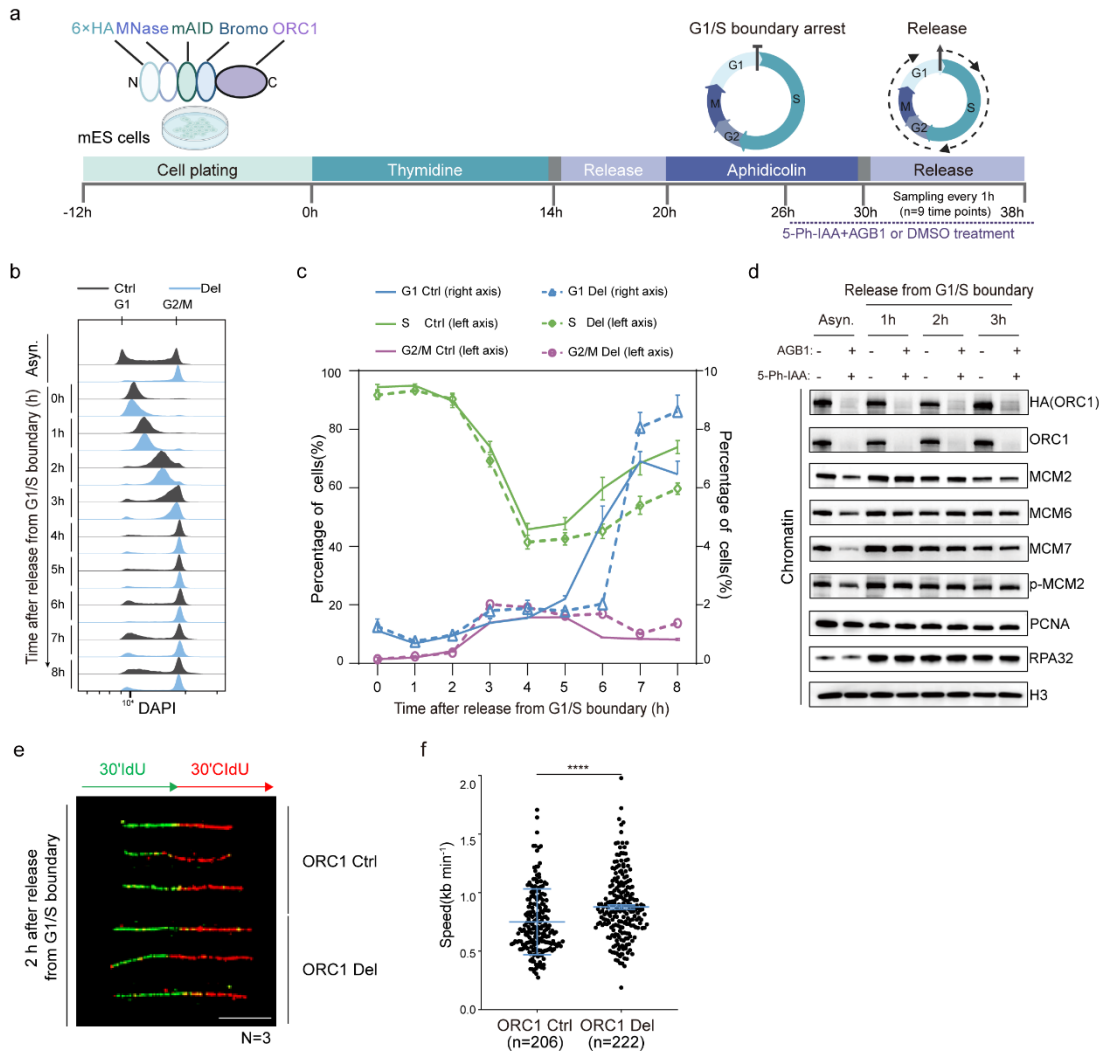

Figure 6. ORC1 is dispensable for DNA replication progression during S phase.

a. Diagram shows the strategy of cell cycle synchronization and release.

b. FACS analysis shows cell-cycle progression after acute depletion of ORC1 during S phase. Asyn., asynchronous cells. Each time point (0-8 h) indicates cells released from thymidine/aphidicolin treatment (G1/S boundary).

c. The statistical analysis of Fig. 6b. The X-axis represents time (hours) after release from G1/S boundary. The left Y-axis indicates the percentage of cells (%) in S phase (green) and G2/M phase (purple), while the right Y-axis indicates the percentage of cells (%) in G1 phase (blue). Solid lines represent control cells, and dashed lines represent ORC1 depletion cells. Data are shown as mean ± SD. n = 3 biological replicates.

d. Western blot results show the levels of chromatin-bound replication factors after acute depletion of ORC1 during S phase. Asyn., asynchronous cells. Each time point (1-3h) indicates cells released from thymidine/aphidicolin treatment (G1/S boundary).

e. DNA fiber assay shows replication fork progression after acute depletion of ORC1 during S phase. Cells were labelled and harvested at 2 h after release from thymidine/aphidicolin treatment (G1/S boundary). N= 3 biological replicates. Scale bar, 10.4 μm.

f. The statistical analysis of Fig. 6e. The X-axis represents the experimental groups. The Y-axis indicates replication

fork speed (kb min^{-1}). Each point represents an individual replication fork, with blue lines marking the median value for each group. **** indicates $p < 0.0001$ (unpaired two-tailed t-test). n = number of fibers analyzed.

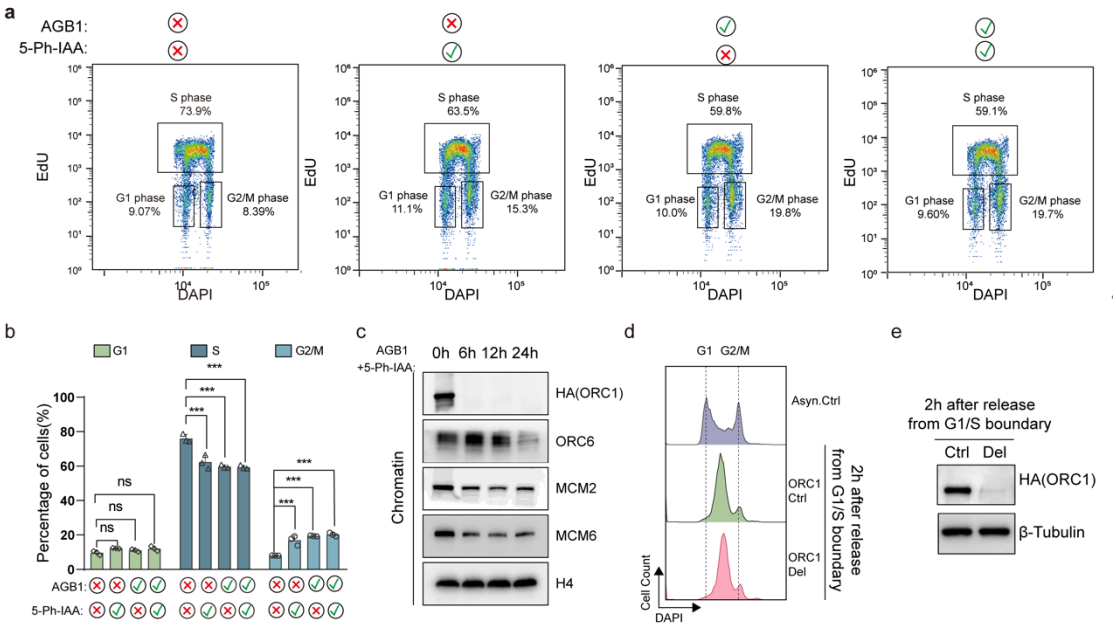

Extended Figure 6. The double-degron system enhances ORC1 depletion and causes severe defects in cell cycle progression.

a. FACS analysis of cell cycle distribution under different treatment conditions (with/without AGB1 and 5-Ph-IAA).

b. The statistical analysis of Extended Fig. 6a. The X-axis represents the four experimental groups, defined by AGB1 and 5-Ph-IAA treatment status. The Y-axis represents the percentage of cells (%), grouped by cell cycle: G1 (green), S (blue), G2/M (cyan). "ns" indicates no significant difference, *** indicates $p < 0.001$ (One-way ANOVA and Dunnett's multiple comparisons test). Data are shown as mean ± SD. n = 3 biological replicates.

c. Western blot results show the levels of chromatin-bound HA-ORC1, ORC6, MCM2 and MCM6 at different time points after AGB1 plus 5-Ph-IAA treatment.

d. FACS analysis shows the efficient synchronization of KI mES cells. Asyn. Ctrl, asynchronous control cells. Control and depletion cells were treated under the same conditions as in Fig. 6e.

e. Western blot results show HA (ORC1) level after AGB1 plus 5-Ph-IAA treatment during S phase.

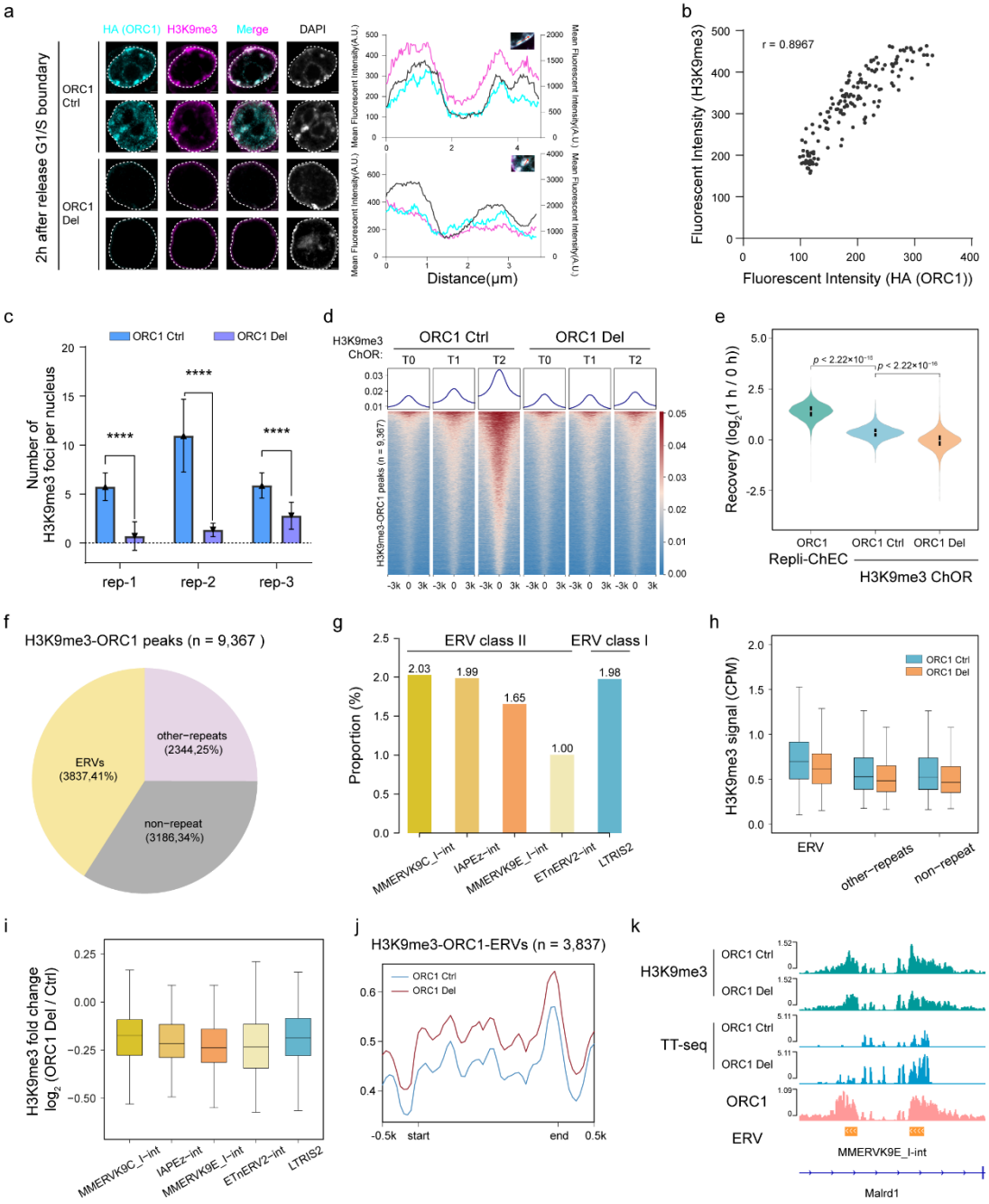

Figure 7. ORC1 regulates H3K9me3 inheritance and ERV silencing during S phase.

a. (Left) IF staining showing the distribution of HA(ORC1) (cyan) and H3K9me3 (magenta) after acute depletion of ORC1 during S phase, with DAPI (white) as a nuclear counterstain. Cells were fixed at 2 h after release from thymidine/aphidicolin treatment (G1/S boundary). ORC1 Ctrl, control cells. ORC1 Del, ORC1-depleted cells. n = 3 biological replicates. Scale bar, 2μm. (Right) The quantification of HA(ORC1), H3K9me3 and DAPI fluorescence intensity along the dotted line as indicated in the insert. The X-axis represents the measured distance (μm). The left Y-axis indicates the average fluorescence intensity of HA(ORC1) (cyan) and H3K9me3 (magenta), while the right Y-axis indicates the average fluorescence intensity of DAPI (black).

b. Dot plot shows the correlation between HA(ORC1) and H3K9me3 foci in nuclei.

c. The statistical analysis of Fig. 7a. The X-axis represents three independent experiments. The Y-axis shows the number of H3K9me3 foci per nucleus (n > 30 cells). **** indicates $p < 0.0001$ (unpaired two-tailed t-test). Data are shown as mean ± SD.

d. Heatmap shows the distribution of H3K9me3 signals across H3K9me3-ORC1 regions on nascent chromatin at different chase time points in control (Ctrl) and ORC1-depleted (Del) cells. Nascent chromatin was collected at 0, 1, 2 h (T0, T1, T2) after thymidine chase following EdU labeling.

e. Violin plot shows the recovery rate (defined as $\log_2$ (1 h / 0 h)) of ORC1 and H3K9me3 signals across the H3K9me3-ORC1 co-localized regions on nascent chromatin (ORC1 repli-ChEC signals and H3K9me3 ChOR signals) in control (Ctrl) and ORC1-deleted (Del) cells.

f. Pie chart shows repeat annotations of H3K9me3-ORC1 co-localized regions.

g. Bar plot shows the most enriched ERV subfamilies within H3K9me3-ORC1 co-localized regions.

h. Box plot shows changes in H3K9me3 signal across H3K9me3-ORC1 co-localized regions upon ORC1 depletion.

i. Box plot shows changes in H3K9me3 signal at the most enriched ERV subfamilies within H3K9me3-ORC1 co-localized regions upon ORC1 depletion.

j. Metaplot shows the distribution of TT-seq signals across ERVs in H3K9me3-ORC1 co-localized regions in control (Ctrl) and ORC1-deleted (Del) cells

k. IGV snapshot shows H3K9me3 and TT-seq signals at *Malrd1* locus in control (Ctrl) and ORC1-deleted (Del) cells

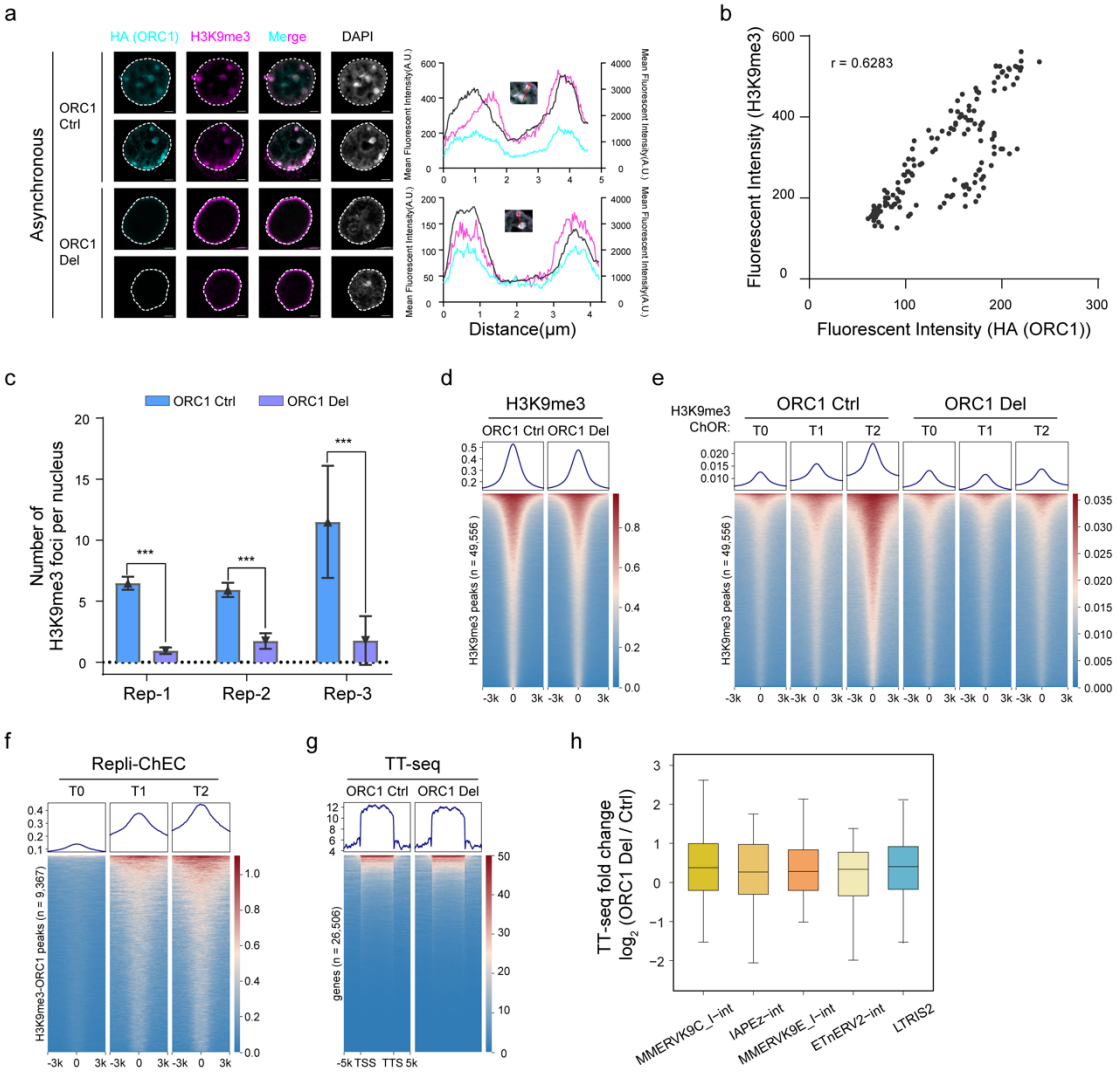

Extended Figure 7. ORC1 coordinates H3K9me3 heterochromatin maintenance and transcriptional repression at ERV regions.

a. (Left) IF staining detecting the distribution of HA(ORC1) (cyan) and H3K9me3 (magenta) in asynchronous cells under indicated treatment conditions, with DAPI (white) as a nuclear counterstain. n = 3 biological replicates. Scale bar, 2μm. (Right) The quantification of HA-ORC1, H3K9me3 and DAPI fluorescence intensity along the dotted line as indicated in the insert. The X-axis represents the measured distance. The left Y-axis indicates the average fluorescence intensity of HA (cyan) and H3K9me3 (magenta), while the right Y-axis indicates the average fluorescence intensity of DAPI (black).

b. Dot plot shows the correlation between HA(ORC1) and H3K9me3 foci in in nuclei.

c. The statistical analysis of Fig. 7a. The X-axis represents three independent experiments. The Y-axis shows the number of H3K9me3 foci per nucleus (n > 50 cells). *** indicates $p < 0.001$ (unpaired two-tailed t-test). Data are shown as mean ± SD.

d. Heatmap shows the distribution of H3K9me3 signals in control (Ctrl) and ORC1-depleted (Del) cells.

e. Heatmap shows the distribution of H3K9me3 signals on nascent chromatin at different chase time points in control (Ctrl) and ORC1-depleted (Del) cells. Nascent chromatin was collected at 0, 1, 2 h (T0, T1, T2) after thymidine

chase following EdU labeling.

f. Heatmap shows the distribution of ORC1 signals across H3K9me3-ORC1 regions on nascent chromatin at different chase time points in control (Ctrl) and ORC1-depleted (Del) cells. Nascent chromatin was collected at 0,1,2 h (T0, T1, T2) after thymine chase following EdU labeling.

g. Heatmap shows the distribution of TT-seq signals in control (Ctrl) and ORC1-depleted (Del) cells.

h. Box plot shows changes in TT-seq signals at the most enriched ERV subfamilies within H3K9me3-ORC1 co-localized regions upon ORC1 depletion.